ORIGINAL PAPER

Analytical estimation of the effective thermal conductivity of a granular bed in a stagnant gas including the Smoluchowski effect

Akhil Reddy Peeketi[1] · Marigrazia Moscardini[2] · Simone Pupeschi[2] · Yixiang Gan[3] · Marc Kamlah[2] · Ratna Kumar Annabattula[1]

Abstract

An analytical model including the Smoluchowski effect to estimate the effective thermal conductivity of a monosized granular assembly with interstitial stagnant gas from the microstructural parameters of the assembly, as well as the bulk properties of the granules and the gas is proposed in this paper. The discrete element method (DEM) is used for the generation and compaction of the granular assemblies. In the granular systems with interstitial gas, heat transfer occurs through the conduction between particles by solid overlap contacts and through the surrounding stagnant gas. Thermal radiation is included in the analytical model to study the influence of radiation on the thermal behavior of the assembly. The effective thermal conductivity is strongly influenced by the pressure of the gas as the conductivity of the gas decreases with decreasing pressure when confined in small gaps. This influence of the gas pressure is implemented in the analytical model. The effect of cyclic loading on the microstructural parameters is investigated through DEM simulations. Parametric correlations are developed to predict the values of microstructural parameters from experimentally measurable parameters so as to bypass any simulations for the estimation of effective thermal conductivity. A good agreement is observed between the analytical model and the experimental results for different assembly parameters and materials. The proposed analytical model can be used to get a first hand estimate of the effective thermal conductivity of a granular assembly to aid in the design process of such systems.
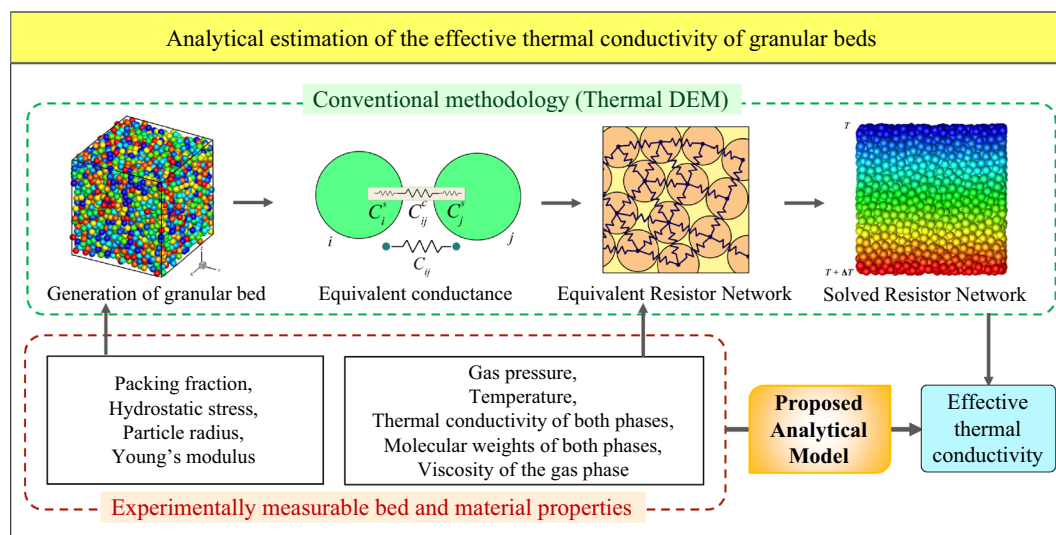
Graphic abstract

Extended author information available on the last page of the article

🖄 Springer

List of symbols

Bulk material properties

p	Porosity of the particle
E	Young's Modulus of solid material (GPa)
ν	Viscosity of gas (Pa s)
Λ	Mean free path of gas (m)
a_c	Accommodation coefficient
γ	Represents amount of energy transfer between the gas molecule and solid material
K_i	Thermal conductivity (W m^{-1} K^{-1}), $i = s, f$
α_0	Bulk conductivity ratio $= K_s/K_f$
m_i	Molecular weight (g mol^{-1}), $i = s, f$
m_r	Molecular weight ratio $= m_s/m_f$
ϵ_r	Emissivity of particle surface

Bed parameters

A	Cross-sectional area of the assembly (m^2)
H	Height of the assembly (m)
$\mathcal{V}$	Total volume of granules in the assembly (m^3)
η_0	Initial packing fraction (packing fraction at the end of three loading/unloading cycles)
η_{RCP}	Packing fraction of assembly as generated by RCP
η	Instantaneous packing fraction
σ_{zz}	Macroscopic stress along the Z-axis (MPa)
ϵ_{zz}	Macroscopic compressive strain along the Z-axis
R	Radius of the particles (m)
D	Diameter of the particles (m)
T	Temperature (K)
P	Gas pressure (Pa)
N_k	Coordination number, $k = o, g$
$\bar{r}_c$	Mean contact radius (m)
h_e	Effective gap (m)
L_k^e	Effective characteristic dimension (m), $k = o, g$
$\bar{\xi}$	Mean dimensionless gap conductance
C^s	Particle conductance (W K^{-1})
C_k^c	Contact conductance (W K^{-1}), $k = o, g$
C_k^e	Effective conductance (W K^{-1}), $k = o, g$
F_r	Radiation exchange factor
k_{eff}	Effective thermal conductivity (W m^{-1} K^{-1})
k_r	Contribution of radiation to the effective conductivity (W m^{-1} K^{-1})
ΔT	Temperature difference applied between top and bottom layers (K)
$\dot{Q}$	Total heat flow rate through the assembly (W)

Interparticle parameters between particles *i, j*

d_{ij}	Distance (m)
h_{ij}	Gap width (m)
$r_{c,ij}$	Contact radius (m)
δ_{ij}	Depth of overlap (m)
θ_{ij}	Contact angle
$L_{k,ij}$	Characteristic dimension (m), $k = o, g$
K_n	Knudsen number

K_f^c	Gas conductivity at contact (W m^{-1}K^{-1})
α_{ij}	Conductivity ratio $= K_s/K_f^c$
β_{ij}	Overlap threshold parameter
λ_{ij}	Gap threshold parameter
ξ_{ij}	Dimensionless gap conductance
$C_{k,ij}^c$	Contact conductance (W K^{-1}), $k = o, g$
C_k^s	Conductance (W K^{-1}) of particle k
C_{ij}	Thermal conductance (W K^{-1})
T_k	Temperature (K) of particle k
$\dot{Q}_{ij}$	Heat flow rate (W)
$\dot{Q}_i$	Heat flow rate (W) between particle i and surroundings

Other symbols

θ, ϕ	Spherical coordinates
ζ	Fitting parameter
ω	$\sin^{-1} \zeta$
R_g	Universal gas constant (8.314 J mol^{-1} K^{-1})
S	Stefan Boltzmann constant (5.67 $\times$ 10^{-8} W m^{-2}K^{-4})

Subscripts

s	Solid phase
f	Fluid phase
o	Overlap type contact
g	Gap type contact

Abbreviations

RN	Resistor network
DEM	Discrete element method
RCP	Random close packing
OSi	Lithium orthosilicate
LMT	Lithium metatitanate
LZT	Lithium metazirconate

1 Introduction

The estimation of effective thermal conductivity of granular-fluid assemblies is of utmost importance for the design of various industrial thermal systems such as solid breeder units in fusion reactors [1, 2], catalytic reactors [3], granular thermal energy storage systems [4] and solid oxide fuel cells [5]. The granular assemblies are multiphase and discrete in nature leading to complex thermo-mechanical coupled systems. The microstructure i.e., the spatial configuration of the particles dictate the effective properties like effective thermal conductivity of the assembly [6]. Further, the effective thermal conductivity (k_{eff}) of the granular assemblies is influenced by various material properties such as thermal conductivities of constituent phases and the other macro properties such as temperature, gas pressure, packing fraction, sizes of the particles etc [7–9].

Extensive experimental investigations have been reported in the literature for estimating k_{eff} of granular beds [10–20]. Conducting such experiments for various materials at different environmental conditions is economically expensive and time consuming, not to mention the possible measurement uncertainty in these experiments. Hence, there is a need for the development of models that can predict the effective conductivity with reasonable accuracy. Numerous models exist in the literature for estimating the effective thermal conductivity of granular beds [6, 21–24]. A few numerical models in the literature include the influence of the spatial configuration of the particles through discrete element or finite element modeling [8, 20, 25, 26]. Discrete element method has also been implemented to model the coupled thermo-hydro-mechanical analysis of granular-fluid assemblies [27]. In some works, the particle-particle contact conditions are taken into consideration and the conductance at each contact is evaluated through contact conductance relations [28–31] in order to estimate the effective thermal conductivity. A few analytical models reported in the literature include the influence of spatial configuration through microstructural parameters (like coordination number, mean contact radius, effective gap etc.) [6, 32, 33]. Most of these analytical models neglect the effect of interstitial gas present in the granular assemblies [32, 33]. The analytical model presented in Peeketi et al. [6] included the effect of gas and the microstructural parameters however they disregarded the effect of the gas pressure. But, the influence of gas pressure on k_{eff} was found to be significant in experiments [13, 15, 19, 34]. This influence of gas pressure on k_{eff} is explained by the dependence of thermal conductivity of gas on its pressure, when the gas is confined in small spaces as in the case of granular beds, known as the Smoluchowski effect [35].

Several numerical models that include the influence of the gas pressure and the spatial configuration of the particles on the effective thermal conductivity are reported in the literature [8, 36–38]. But there are only a few analytical models that include the effect of gas pressure on the effective thermal conductivity of a granular assembly [39, 40]. However, these models do not include the effect of the spatial configuration of the granular assembly that influences the effective thermal conductivity [40]. The analytical models that include effect of microstructural parameters need simulations for the generation of granular assemblies to estimate the microstructural parameters [6, 33]. The aim of this work is to develop an analytical model to predict the effective thermal conductivity of a granular assembly

- including the influence of the material properties of both solid and gas, as well as macro-properties such as packing fraction, temperature, gas pressure and the spatial configuration of the assembly characterized by microstructural parameters

- by estimating the microstructural parameters needed for the analytical model through parametric correlations instead of having to obtain the microstructure information from additional simulations such as the discrete element method (DEM).

In this paper, the numerical approach (based on the Resistor Network (RN) model) and the analytical model proposed in Peeketi et al. [6] for monosized spherical granular assemblies are further improved to include the Smoluchowski effect with inspiration from the numerical model proposed in Moscardini et al. [8]. Both the numerical and analytical models are presented in Sect. 2. The contact conductance relations used to evaluate the contact conductance between neighboring particles are thoroughly explained in Sect. 2.2. The formulation to include the Smoluchowski effect in estimating the thermal conductivity of gas at the contacts is presented in Sect. 2.3. Since the interstitial gas is considered to be stagnant, the heat transfer due to convection is neglected in this work. The bed is assumed to be in steady state (i.e. particles neither generate any heat nor change temperature over time). At the end of Sect. 2, the proposed analytical model still depends on the DEM simulations to evaluate the required microstructural parameters. Therefore, in Sect. 3, a set of parametric correlations for the microstructural parameters are developed from the numerical characterization of assemblies (through DEM simulations) to propose a fully analytical approach. Finally, the proposed analytical model is compared with the experimental results for different materials and assembly parameters in Sect. 4.

2 Models for the estimation of effective conductivity

2.1 Numerical model

The steady state RN model (numerical approach) proposed in [6] is further developed to include the Smoluchowski effect. A pebble bed is a multiphase system with gas in the interstitial voids created by the spatial configuration of pebbles. The heat transfer between the pebbles takes place through two heat transfer paths, namely the pebble-pebble mechanical contact area and the gas surrounding the pebbles as shown in the Fig. 1a, b [6]. In our approach, two spherical particles are in mechanical contact if their centers are closer than the sum of their radii. In this case, their ideal spherical shapes would be overlapping for which reason we denote in the following a mechanical contact as overlap contact. The heat flow rate $\dot{Q}_{ij}$ between the two particles i and j is

$$\dot{Q}_{ij} = C_{ij}(T_i - T_j). \tag{2.1}$$

(a)   **(b)**   **(c)**
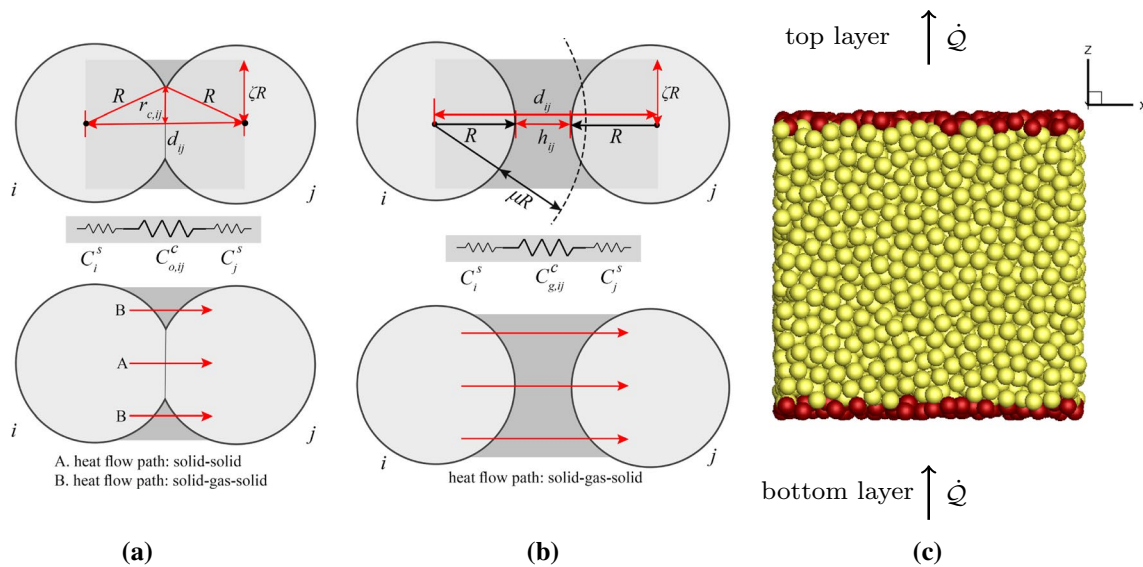
Fig. 1 **a**, **b** Schematic showing the equivalent model for the inter-particle conductance for (**a**) an overlap type contact between neighboring particles i and j along with the corresponding heat flow path and (**b**) a gap type contact between neighboring particles i and j along with the corresponding heat flow path. **c** Schematic showing the axial heat flow direction for a sample assembly. The top and bottom layers are colored red for reference (color figure online)

where C_{ij} is the thermal conductance between the particles i and j, T_i and T_j are the temperatures of particles i and j, respectively. The thermal conductance C_{ij} is dependent on the type of contact, the details of which are discussed in Sect. 2.2. The thermal conductivity of the gas at each contact is estimated considering the influence of the gas pressure (see Sect. 2.3). The sum of the heat flows entering and leaving the particle i must be zero as it is neither generating nor accumulating any heat. Hence,

$$\sum_j \dot{Q}_{ij} + \dot{Q}_i = 0, \tag{2.2}$$

where $\dot{Q}_i$ is the heat flow rate between the particle i and the surroundings of the assembly. In this work, a representative volume element (RVE) from a large granular assembly is considered for the analysis. The RVE thus has mechanical periodic boundary conditions in all the three directions and thermal periodic conditions on the lateral sides with a temperature gradient in the z direction representing one-dimensional heat flow. The periodic thermal conditions on the lateral sides implies net heat transfer in lateral sides is zero. Hence, $\dot{Q}_i$ will be zero for every particle i other than the top and bottom layers. The temperature of the top and bottom layers of granules are prescribed depicting the axial heat flow direction as shown in Fig. 1c.

Equations 2.1 and 2.2 result in a system of linear equations that is solved to obtain the unknown temperatures and heat flows entering/leaving the particles to the surroundings. The total heat flow through the granular assembly is estimated as

the sum of all the heat flows entering/leaving the assembly. If $\dot{Q}$ is the total heat entering/leaving the assembly, A is the cross-sectional area of the granular assembly, ΔT is the temperature difference applied between the top and bottom layers and H is the distance between the top and bottom layers, then the effective conductivity k_{eff} is given by

$$k_{\text{eff}} = \frac{\dot{Q}}{A} \frac{H}{(\Delta T)}. \tag{2.3}$$

The formulation used for estimating the contact conductance (C_{ij}) is presented in the following.

2.2 Conductance relations

Adjacent particles in the granular assembly are considered to possess two types of contacts—overlap and gap. The overlap and gap type contacts between the particles i and j are characterized by the contact radius $r_{c,ij}$ and the gap width h_{ij}, respectively. If R is the radius of granules and d_{ij} is the distance between centers of particles i and j, then

$$h_{ij} = d_{ij} - 2R \text{ and } r_{c,ij} = \sqrt{\frac{|h_{ij}|R}{2}}. \tag{2.4}$$

The neighboring particles are considered to be in gap type contact when the gap width h_{ij} between them is in the range (0 to μR). If gap width h_{ij} is less than 0, then they are considered as overlap type contact particles. Figure 1a, b illustrates the particle contact condition. The cutoff factor (μ) is

chosen as 0.5 as it was observed to agree with the experimental results [6, 8, 25, 41]. As the particle conductance (C_i^s, C_j^s) and the contact conductance C_{ij}^c are in series, the thermal conductance (C_{ij}) between the particles i and j is given by

$$\frac{1}{C_{ij}} = \frac{1}{C_i^s} + \frac{1}{C_{ij}^c} + \frac{1}{C_j^s}. \tag{2.5}$$

In this work, we use the modified contact conductance relations [6, 8] obtained from the original relations proposed by Batchelor and O'Brien [28]. If K_s and K_f^c are the bulk conductivities of solid and fluid, respectively at the contact, then the conductance of each type of contact can be formulated as below,

- Conductance between the overlapped particles i and j with contact radius ($r_{c,ij}$)

$$C_{o,ij}^c = \pi K_f^c R [H_c + \Delta H_g + \ln(\alpha^2)], \tag{2.6}$$

  where $H_c = 0.22\beta_{ij}^2$ and $\Delta H_g = -0.05\beta_{ij}^2$ for $\beta_{ij} < 1$; $H_c = 2\beta_{ij}/\pi$ and $\Delta H_g = -2\ln(\beta_{ij})$ for $\beta_{ij} > 100$ and a linear interpolation is used for $1 < \beta_{ij} < 100$. Note that, $\beta_{ij} = (\alpha_{ij} r_{c,ij})/R$ and $\alpha_{ij} = K_s/K_f^c$.

- Conductance between the neighboring particles i and j with gap width (h_{ij})

$$C_{g,ij}^c = \pi K_f^c R [\, (1 - \lambda_{ij}) \ln(\alpha^2) \\ + \lambda_{ij} \ln(1 + \alpha^2 \zeta^2) \,], \text{ for } \lambda_{ij} < 1, \tag{2.7a}$$

$$C_{g,ij}^c = \pi K_f^c R \xi_{ij} \text{ otherwise}, \tag{2.7b}$$

  where $\xi_{ij} = \ln(1 + \zeta^2 R/h_{ij})$, $\lambda_{ij} = (\alpha_{ij}^2 h_{ij})/R$, $\alpha_{ij} = K_s/K_f^c$ and ζ is the fraction of the mean radius R [41] considered for the gaseous heat transfer.

The particle conductance (C^s) i.e., the conductance due to the half sphere is given by [41]

$$C_i^s = C_j^s = C^s = \frac{\pi K_s (\zeta R)^2}{R}. \tag{2.8}$$

The value of ζ varies between 0 and 1 and can be picked to match the model with the experimental measurements [8, 25, 41]. An educated guess can be made for the value of ζ based on the solid to gas conductivity ratios. The exact value of ζ for different solid to gas conductivity ratios is determined through trial and error which will be discussed in Sect. 4.

2.3 Implementation of the Smoluchowski effect

The analytical model developed in [6] includes the effect of microstructural parameters such as overlap coordination number (N_o), gap coordination number (N_g), mean contact radius ($\bar{r}_c$), effective gap (h_e) and packing fraction (η) in addition to the particle diameter (D) and the bed temperature (T). But their model doesn't include the effect of the surrounding gas pressure on the effective conductivity. The conductivity of the gas decreases with decreasing pressure in small confined spaces where the mean free path of the gas is of the order of the characteristic dimension of the gap. This phenomena is termed as Smoluchowski effect [35]. The mean free path of the interstitial gas molecules increases with the decrease in pressure at a given temperature. As a result, when the mean free path of the gas molecules reaches the order of magnitude of the geometrical dimension of the gas confinement, the thermal conductivity of the gas becomes dependent on its pressure. The thermal conductivity of the gas is independent of the pressure as long as the mean free path is much smaller than the dimensions of confinement. In order to include the influence of pressure on the effective conductivity, the value of the conductivity of the gas to be used in the contact conductance relations needs to be modified to account for Smoluchowski effect.

The significance of the effect of the gas pressure on the thermal conductivity of the gas is decided by the Knudsen number ($K_n = \Lambda/L$) defined as the ratio of mean free path of the gas (Λ) and the characteristic dimension of the confinement (L) estimated using the gap between two neighbouring particles (see the last part of Sect. 2.3 for details). For very low Knudsen number ($K_n < 0.001$), the gas thermal conductivity is independent of the pressure and equal to the unconfined value. For $0.001 < K_n < 10$, the thermal conductivity of the gas decreases with decrease in pressure as the mean free path approaches the order of magnitude of the characteristic dimension of the confinement and the heat transfer becomes less effective. For $K_n > 10$, the collision between molecules can be neglected and the thermal energy is transferred by direct collision of gas molecules with the solid phase. The thermal conductivity of the gas phase is very low and is independent of the gas pressure in this regime.

The accounting for the Smoluchowski effect in the estimation of k_{eff} using the DEM code was first presented by Moscardini et al [8]. In this work, we use a similar framework for the estimation of the gas conductivity at each contact. The thermal conductivity of the gas (K_f^c) at a contact can be estimated using the relation given by Kaganer [42] as,

$$K_f^c = \frac{K_f}{1 + 2\gamma K_n}, \tag{2.9}$$

where K_f is the bulk gas conductivity, K_n is the Knudsen number and γ represents the amount of energy transfer between the gas molecule and solid material. In this work,

the mean free path of the gas is estimated in terms of viscosity rather than the kinetic molecular diameter, as in [8], since the viscosity provides a better estimate of mean free path for the real gases. In general, the kinetic molecular diameter and mean free path of a gas are actually estimated from their relationship with the viscosity of a gas, an experimentally measurable quantity [43, 44]. The effect of temperature on the mean free path of a gas is not included in Moscardini et al. [8] and they use a constant value of kinetic molecular diameter for different gas temperatures. In this work, the effect of temperature on the mean free path of the gas is included by considering the relationship between mean free path and gas viscosity resulting in a better accuracy of the model. The mean free path of the gas can be estimated in terms of viscosity as

$$\Lambda = \frac{\nu}{P}\sqrt{\frac{\pi R_g T}{2m_f}}, \tag{2.10}$$

where ν is the viscosity of the gas, P is the gas pressure, m_f is the molecular weight of gas, T is the temperature of gas and R_g is the universal gas constant. The correlation proposed by Wawryk and Rafalowicz [45] is used for the estimation of γ as [46]

$$2\gamma = \left(\frac{19}{6}\right)\frac{2 - a_c}{a_c} \tag{2.11}$$

where a_c is the thermal accommodation coefficient representing the effectiveness of the energy transfer between the solid and the gas given by

$$a_c = \frac{2.4m_r}{(1 + m_r)^2}. \tag{2.12}$$

here m_r is the ratio of molecular weights of solid and gas phase ($m_r = m_s/m_f$). In general, the accommodation coefficient is a function of temperature and needs to be measured experimentally for each gas type and solid material [46] as a function of temperature. In this work, we neglect the dependency of a_c on temperature and use Eq. 2.12 as it best matches with the experimental observations reported by Goodman [46].

2.3.1 Estimation of characteristic dimension (L)

The characteristic dimension is estimated by taking the mean of the gap between two contacting particles over the azimuthal angle (ϕ) range of 0–2π and polar angle (θ) range depending on the type of contact. For an overlap type contact, the range for the polar angle is $\theta_{c,ij}$ to ω whereas for a gap type contact, it is 0 to ω as shown in Fig. 2. Here, $\theta_{c,ij}$ is the overlap contact angle defined as $\theta_{c,ij} = \sin^{-1}(r_{c,ij}/R)$ and ω is defined as $\omega = \sin^{-1}\zeta$.
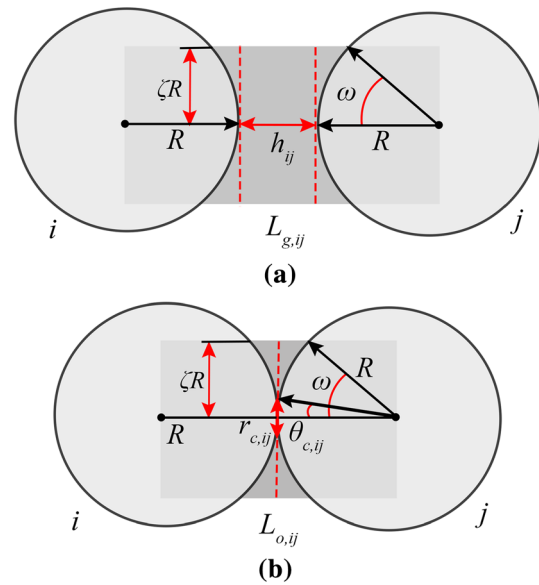
Fig. 2 Schematic showing the range of polar angle for **a** a gap type contact and **b** an overlap type contact
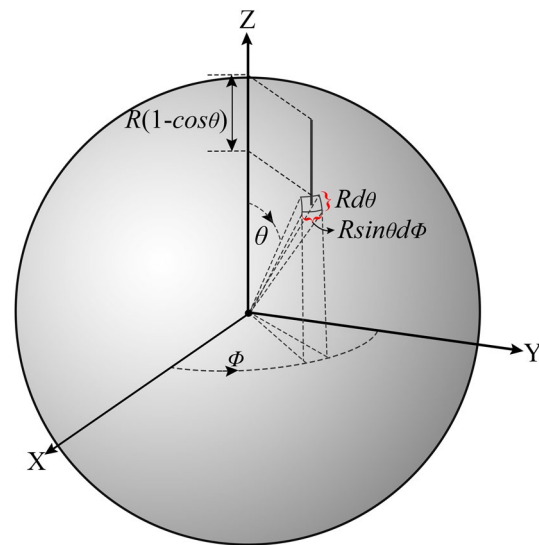
Fig. 3 Schematic showing the segment $R(1\text{-cos}\,\theta)$ for a given (θ, ϕ)

The characteristic gap dimension $L_{g,ij}$ can be formulated as the sum of the gap width (h_{ij}) and the average of the segment $R(1\text{-cos}\,\theta)$ for a given (θ, ϕ) as shown in Fig. 3. Therefore, $L_{g,ij}$ can be written as,

$$L_{g,ij} = 2\frac{\int_0^{2\pi}\int_0^{\omega} R(1 - \cos\theta)R^2 \sin\theta \, d\theta d\phi}{\int_0^{2\pi}\int_0^{\omega} R^2 \sin\theta \, d\theta d\phi} + h_{ij} \tag{2.13}$$

$$= R(1 - \cos\omega) + h_{ij}.$$

For the case of an overlap type contact between particles i and j, the segment would be $R(1\text{-}\cos\theta) - \delta_{ij}/2$ with δ_{ij} as the depth of contact given as $\delta_{ij} = 2R - d_{ij} = r_{c,ij}^2/R$ as shown in the Fig. 4. Therefore, the characteristic overlap dimension $L_{o,ij}$ can be written as

$$L_{o,ij} = 2\frac{\int_0^{2\pi}\int_{\theta_{c,ij}}^{\omega}(R(1-\cos\theta) - \delta_{ij}/2)R^2\sin\theta\,d\theta d\phi}{\int_0^{2\pi}\int_{\theta_{c,ij}}^{\omega}R^2\sin\theta\,d\theta d\phi} \quad (2.14)$$

$$= R(2 - \cos\theta_{c,ij} - \cos\omega) - \delta_{ij}.$$

The values of $L_{g,ij}$ and $L_{o,ij}$ are used to calculate the respective Knudsen numbers (K_n) for each contact. Then, the thermal conductivity of the gas at each contact, K_f^c, estimated using Eq. 2.9 is substituted into the contact conductance relations given by Eqs. 2.6 and 2.7. Finally, the conductance between the neighboring particles (C_{ij}) is calculated using Eq. 2.5 which will be used to estimate k_{eff} numerically as described in Sect. 2.1. The estimation of k_{eff} by the RN model presented in Sect. 2.1 using the conductance formulations described in Sects. 2.2, 2.3 and introduced in [6, 8] is referred to as the numerical model in the following.

2.4 Analytical model

In this section, the analytical model proposed in [6] for the estimation of k_{eff} for granular assemblies is briefly discussed. The effective thermal conductivity of a monosized isotropic granular assembly in a gaseous environment is given by [6]
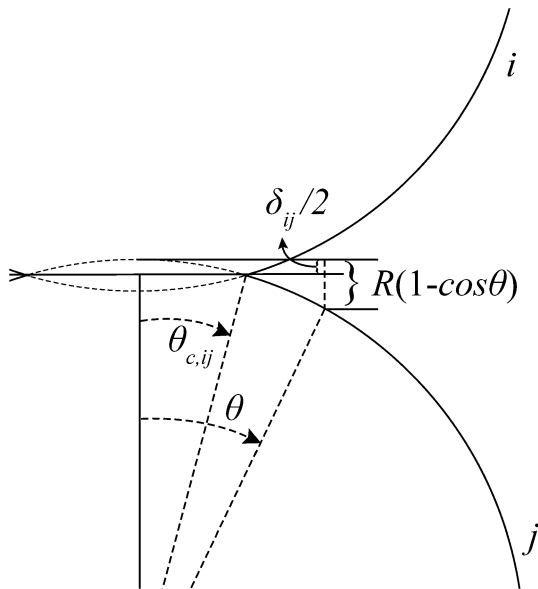
Fig. 4 Schematic showing the estimation of characteristic dimension for overlap type contact

$$k_{\text{eff}} = \frac{\eta(N_o C_o^e + N_g C_g^e)}{\pi D}. \quad (2.15)$$

here η is the packing fraction of the assembly, D is the mean diameter of the particles, N_o, N_g are the mean overlap and gap coordination numbers. C_o^e, C_g^e are the effective overlap and gap contact conductances given by,

$$\frac{1}{C_i^e} = \frac{1}{C^s} + \frac{1}{C_i^c} + \frac{1}{C^s}, \text{ for } i = o, g, \quad (2.16)$$

where C_o^c, C_g^c are contact conductances of overlap and gap type contacts respectively. C_o^c and C_g^c are estimated using the contact conductance relations described in Sect. 2.2. C_o^c is estimated using the mean contact radius ($\bar{r}_c$) whereas the effective gap (h_e) is used for estimating the C_g^c which can be estimated by [6]

$$h_e = \frac{\zeta^2 R}{\exp(\bar{\xi}) - 1}, \quad (2.17)$$

where $\bar{\xi} = \langle \ln(1 + \zeta^2 R/h_{ij}) \rangle$, where $\langle \cdot \rangle$ indicates the mean of the enclosed ($\cdot$) quantity. Since, the gap threshold parameter $\lambda_{ij} = (\alpha_{ij}^2 h_{ij})/R$ depends on the solid to gas conductivity ratio (α_{ij}), the value of $\bar{\xi}$ also depends on the solid to gas conductivity ratio. To eliminate this dependency, only the gap contacts with normalized gap width (h_{ij}/R) greater than 10^{-4} are considered for the estimation of $\bar{\xi}$, which is needed to calculate the effective gap (h_e) of the assembly. The number of gap type contacts with normalized gap width (h_{ij}/R) less than 10^{-4} are almost negligible, but even such low number of contacts affect the estimation of h_e due to the logarithmic nature of ξ. Also, the contacts with normalized gap width (h_{ij}/R) less than 10^{-4} usually fall into the category of touch type contact [6, 28] and their contribution to the effective conductivity is negligible [6]. The step by step procedure for estimating k_{eff} using the analytical formulations discussed in Sects. 2.2–2.4 is presented in the following.

2.5 Calculation of the effective conductivity using the analytical model

The steps involved in calculating the effective thermal conductivity (k_{eff}) through the analytical model from the bulk material properties as well as microstructural parameters are presented in the form of flow chart in Fig. 5. The analytical estimation of k_{eff} using Eq. 2.15 requires the specification of values of the instantaneous packing fraction (η), particle radius (R), overlap and gap coordination numbers (N_o, N_g), effective overlap and gap conductances (C_o^e, C_g^e). The values of η, N_o and N_g can be obtained directly from the DEM simulations. The values of C_o^e and C_g^e are calculated using Eq. 2.16 from the corresponding contact conductance (C_o^c, C_g^c) and
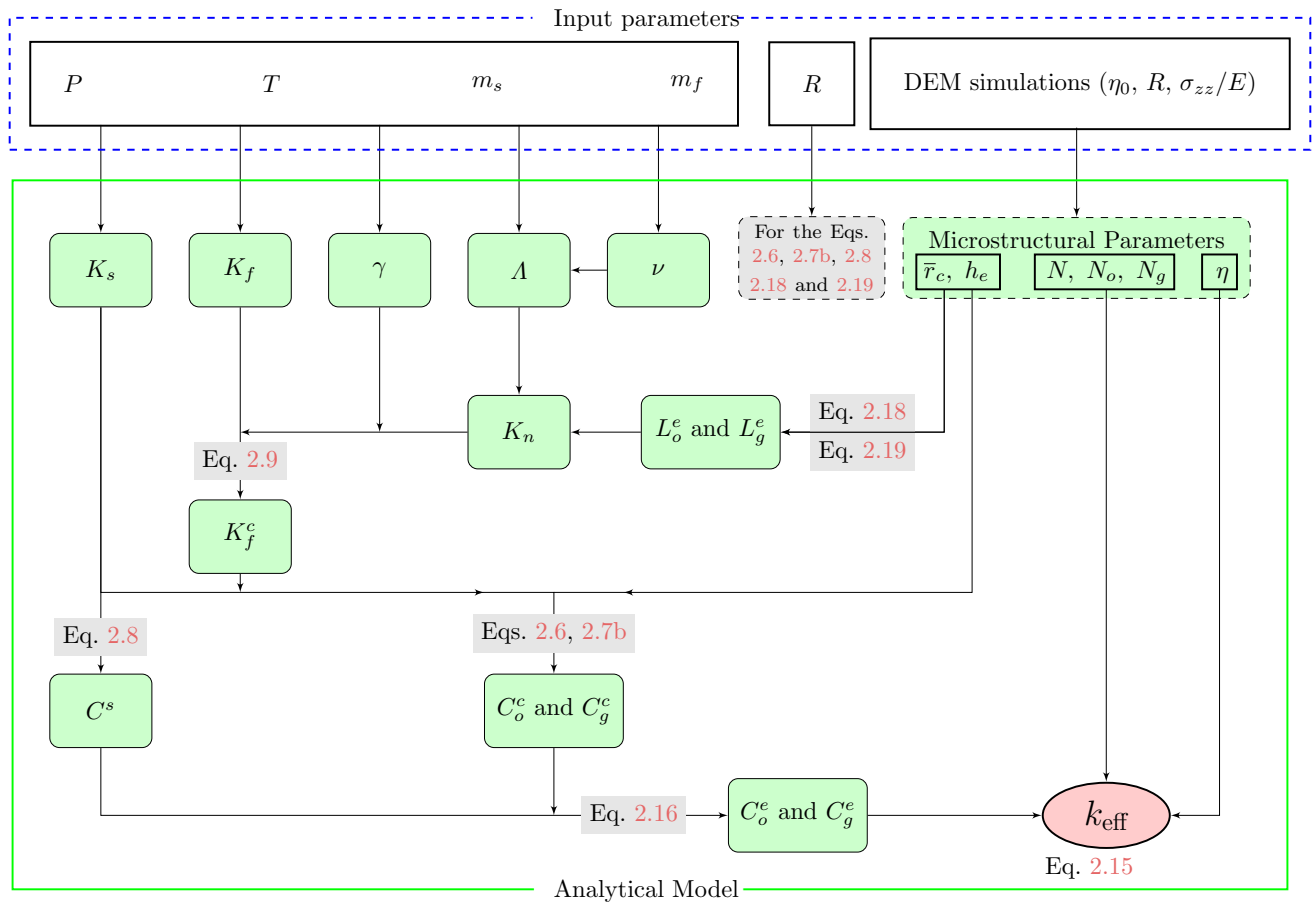
Fig. 5 Flow chart for the calculation of k_{eff} through the analytical model

the particle conductance (C^s) values. The value of C^s is estimated using Eq. 2.8 as a function of the particle radius (R) and the solid conductivity (K_s). The value of C_o^c is calculated using Eq. 2.6 by substituting the value of the mean contact radius ($\bar{r}_c$) in the place of $r_{c,ij}$, whereas, the value of C_g^c is calculated using Eq. 2.7b by substituting the value of the effective gap (h_e) in the place of h_{ij}. The values of $\bar{r}_c$ and h_e are obtained from the DEM simulations. Furthermore, the Eqs. 2.6 and 2.7b also require the specification of values of the solid conductivity (K_s) and the gas conductivity at contact (K_f^c). The value of K_f^c is calculated for overlap and gap type contacts from their corresponding Knudsen numbers (K_n) and the bulk gas conductivity (K_f) values using Eq. 2.9. The Knudsen number corresponding to overlap contact depends on the effective characteristic overlap dimension (L_o^e) as $K_n = \Lambda/L_o^e$, whereas the Knudsen number corresponding to gap contact depends on the effective characteristic gap dimension (L_g^e) as $K_n = \Lambda/L_g^e$. Note that the estimation of K_n requires the specification of mean free path of the gas Λ. The value of L_o^e is estimated from $\bar{r}_c$ as

$$L_o^e = R(2 - \cos\bar{\theta}_c - \cos\omega) - \bar{r}_c^2/R, \tag{2.18}$$

where $\bar{\theta}_c$ is the mean overlap contact angle defined as $\bar{\theta}_c = \sin^{-1}(\bar{r}_c/R)$ and $\omega = \sin^{-1}\zeta$. The value of L_g^e is estimated from h_e as

$$L_g^e = R(1 - \cos\omega) - h_e. \tag{2.19}$$

The values of bulk solid and gas conductivities (K_s, K_f) are evaluated as a function of bed temperature (T). The value of the mean free path of the gas is calculated as a function of viscosity of gas (ν), temperature (T), gas pressure (P) and molecular weight of gas (m_f) using Eq. 2.10. The viscosity of gas ν is evaluated as a function of temperature (T). The value of γ used in estimating K_f^c (Eq. 2.9) is calculated using Eq. 2.11 from the accommodation coefficient (a_c) which is evaluated in terms of the solid to gas molecular weight ratio (Eq. 2.12). To provide values of the microstrcutural parameters, the DEM simulations require the specification of input parameters such as the initial packing fraction (η_0), normalized macroscopic stress (σ_{zz}/E) and the particle radius (R) (discussed in Sect. 3).

The analytical model is compared with the numerical results for different cases and shown in Fig. 6. The
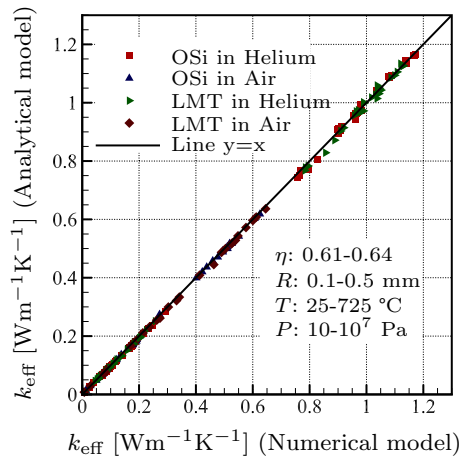
Fig. 6 Comparison of k_{eff} evaluated from the numerical model with that of k_{eff} calculated from the analytical model with microstructural parameters estimated from DEM simulations for different granular assembly parameters

numerical results have been obtained by considering the contact conductance for each individual contact as described in Sects. 2.1–2.3. The material properties are presented in Table 1. The numerical and the analytical models show a good agreement as seen in Fig. 6. The analytical model presented so far is still dependent on the DEM simulations to obtain the microstructural parameters (η, N_o, N_g, $\bar{r}_c$, h_e). In Sect. 3.2, we attempt to develop parametric correlations for the microstructural parameters to completely eliminate the dependence on DEM simulations for the analytical model.

2.6 Contribution of radiation to the effective conductivity

The contribution of radiation to the effective thermal conductivity of the bed can be approximated as heat transfer parallel to conduction. So, the conductivity due to radiation (k_r) can be directly added to the estimated k_{eff}. The conductivity due to radiation can be taken as [38]

$$k_r = 4F_r D S T^3, \tag{2.20}$$

where S is the Stefan-Boltzmann constant and T is the temperature [K] of assembly and F_r is the radiation exchange factor. The radiation exchange factor F_r cannot be calculated easily and depends on different bed properties such as emissivity of the particle surface (ϵ_r), packing fraction (η), dimensionless solid conductivity etc [22]. Different correlations were proposed in the literature for the estimation of F_r [22]. In this work, correlation given by Wakao and Kato [47] for F_r as

$$F_r = \frac{2}{2/\epsilon_r - 0.264}, \tag{2.21}$$

is used. A value of 0.5 is used for ϵ_r in this work for all the solid materials as suggested by Asakuma et al. [48]. This approach is a very simple approximation to account for the contribution of radiation to the effective thermal conductivity of a granular assembly [22].

3 Development of parametric correlations for microstructural parameters through DEM simulations

The discrete element method (DEM) is a numerical method to simulate the physical response of a system consisting of discrete particles as in the case of granular beds [49]. In this work, we assume all the particles to be spherical and elastic. Every single particle is considered to be independent of any other particle in the system unless it is in mechanical contact with any of them. Hertzian contact mechanics [50] is implemented for simulating the normal contact forces on the contacting particles depending on the elastic properties of each contacting particle.

The Random Close Packing (RCP) algorithm [51] has been used to generate initial granular assemblies with 5000 monosized particles in each assembly. Such a random close packing assembly is then subjected to compression along the axial direction using DEM (as developed in [52, 53]) where we obtain the new configurations of the assembly with respect to the strain applied. The DEM simulations are performed with periodic boundary conditions on all sides to ensure a bulk response of a random packing in the total volume. The experimental studies on the packing fraction of granular assemblies showed that the packing fraction obtained through pouring and tapping falls in the range of 0.60–65 [54, 55]. Hence, in this work, the granular assemblies are generated with different initial packing fractions in the range of 0.61–0.65. The RCP algorithm is used to generate assemblies with desired packing fractions ($\eta_{RCP} \approx 0.61, 0.62, 0.63$ and 0.64). The granular assemblies as obtained from the RCP are compressed up to ≈ 6 MPa macroscopic stress (σ_{zz}) along the Z-axis (see Fig. 7) for ten loading/unloading cycles. The stress-strain response for the cyclic loading is shown in Fig. 8a. The effect of compression on the microstructural parameters is studied in [6] for a single loading. The influence of cyclic loading on the microstructural parameters (η, N_o, N_g, $\bar{r}_c$, h_e) for ten loading/unloading cycles is presented in the following.

3.1 Effect of cyclic loading on the microstructural parameters

Figures 8 and 9 show the effect of cyclic compressive loading on different parameters of a granular assembly. The instantaneous packing fraction (η) of an assembly is
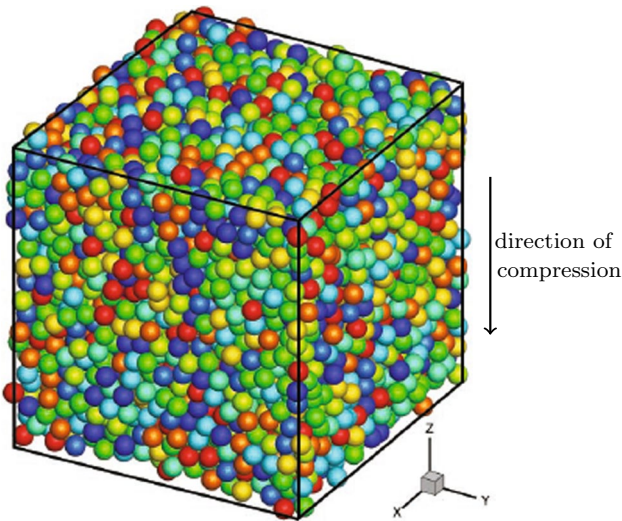
Fig. 7 Schematic showing a sample 3D granular assembly and the direction of the applied compressive force in DEM simulations

estimated as $\eta = \mathcal{V}/(AH)$, where $\mathcal{V}$ is the total volume of the granules, A is the cross-sectional area and H is the height of the assembly. For the present system, it can be stated that

$$\delta\eta/\eta = -\delta H/H = \epsilon_{zz}, \qquad (3.1)$$

as $\mathcal{V}$ and A are constant with compression for the given assembly. Here, ϵ_{zz} is the macroscopic compressive strain of the assembly. Hence, both stress-strain and stress-η show equivalent relationship as seen in Fig. 8a, b for loading/unloading cycles. Figure 9a shows the variation of coordination numbers with σ_{zz} for 1, 2, 4, 7 and 10 loading/unloading cycles. It can be observed from Fig. 9a that the total coordination number (N) is constant with cyclic loading insinuating that the particle rearrangements are local in nature. As the assembly is compressed, gap type contacts transform to overlap type contacts. So, the overlap coordination number (N_o) increases with increasing macroscopic stress and the gap coordination number (N_g) decreases with increasing macroscopic stress. Also, some of the gap contacts that

Fig. 8 a The stress-strain response of a sample assembly for 10 loading/unloading cycles, **b** Effect of cyclic loading on instantaneous packing fraction (η) as a function of macroscopic stress σ_{zz}. (The plots in the figures correspond to an assembly with $\eta_{RCP} = 0.63$, $R = 250\,\mu m$ and $E = 90\,GPa$ for the first, second, fourth, seventh and tenth loading/unloading cycles. Arrows in the figures indicate the loading/unloading cycle numbers in the increasing order)

(a)

(b)
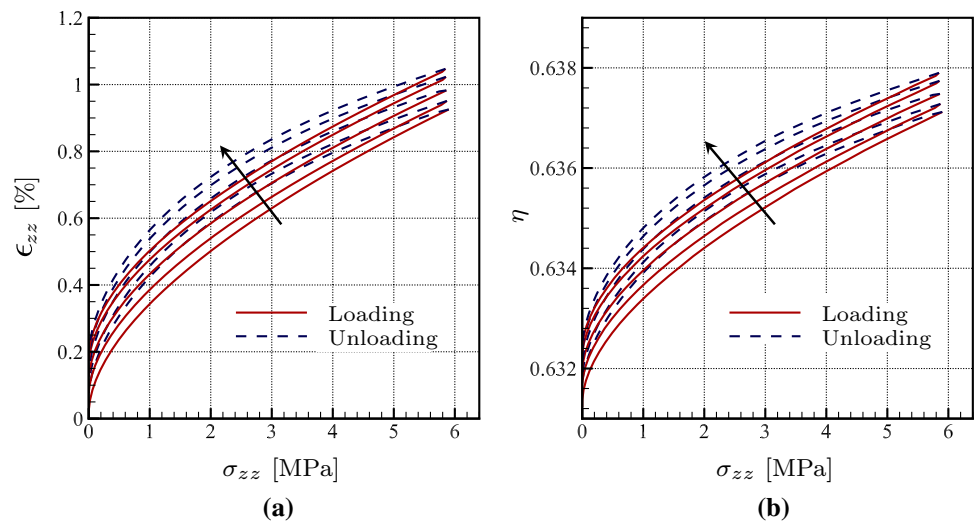
Fig. 9 Effect of cyclic loading on **a** coordination numbers N, N_o, N_g **b** normalized mean contact radius $\bar{r}_c/R$ as a function of macroscopic stress σ_{zz}. (The plots in the figures correspond to an assembly with $\eta_{RCP} = 0.63$, $R = 250\,\mu m$ and $E = 90\,GPa$ for the first, second, fourth, seventh and tenth loading/unloading cycles. Arrows in the figures indicate the loading/unloading cycle numbers in the increasing order)

(a)

(b)
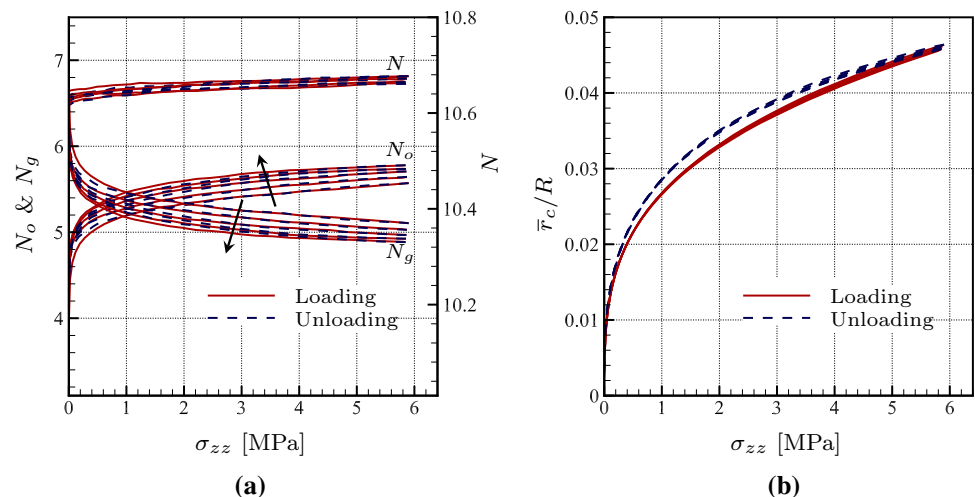
Fig. 10 Effect of cyclic loading on **a** normalized effective gap h_e, **b** effective conductivity k_{eff} as a function of macroscopic stress σ_{zz}. (The plots in the figures correspond to an assembly with $\eta_{RCP} = 0.63$, $R = 250\,\mu\text{m}$ and $E = 90\,\text{GPa}$ for the first, second, fourth, seventh and tenth loading/unloading cycles. Arrows in the figures indicate the loading/unloading cycle numbers in the increasing order)
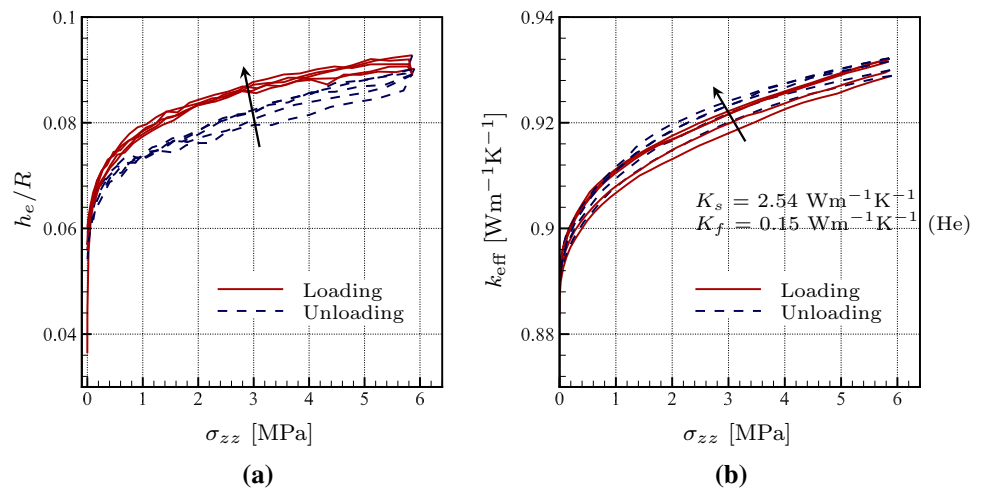
transformed to overlap contacts during the loading don't transform back to gap contacts during unloading. This results in slightly higher N_o in unloading than loading as can be observed in Fig. 9a. Hence, each loading/unloading cycle generates residual overlap contacts resulting in an overall increase in N_o and an overall decrease in N_g with more cycles. However, the increase in overlap coordination numbers and the decrease in gap coordination numbers seem to reduce with the increasing number of cycles as shown in Fig. 9a indicating that the major particle rearrangements are limited to first few cycles. The normalized mean contact radius ($\bar{r}_c/R$) almost retraces the same path for every cycle as seen in Fig. 9b. This may be due to the compact nature of assemblies ($\eta > 0.61$) prohibiting the large rearrangements and the elastic nature of the spheres as assumed in the DEM simulations. Also, higher $\bar{r}_c/R$ for unloading than loading might be the result of residual strain of the assembly. During loading, gap contact pairs having the least gap width transform to overlap contacts leaving out the number of gap contacts with higher gap width in the assembly almost unchanged. In addition, the gap width of the existing gap type contacts decreases with increase in compression, but not enough to compensate the loss of lower gap width contacts to overlap contacts. The above two contrasting phenomena result in a slight increase in the effective gap of the assembly with the increase in compressive stress as shown in Fig. 10a. A similar observation on the transformation of gap to overlap type contacts has been reported by Peeketi et al. [6]. The RCP algorithm generates assemblies with least possible mechanical contacts. However, the particles of RCP assembly will be closer to each other resulting in low effective gap at the start of first loading as seen in Fig. 10a. All the particles which came closer during loading do not necessarily revert back to their original gap width during unloading stage resulting in a lower effective gap during unloading than loading as shown in Fig. 10a. However, the variations in effective gap (h_e) with increasing number of cycles seem

to be low as can also be seen in Fig. 10a. Figure 10b shows an increase in the effective thermal conductivity (k_{eff}) with increase in compressive stress. As major variations in microstructural properties that define k_{eff} occur during the first few cycles, the variations in k_{eff} are also limited to first few cycles. The variations in k_{eff} almost saturate with the fourth loading/unloading cycle as seen in Fig. 10b indicating the saturation in major local rearrangements of particles. This insight supports the "mechanical conditioning" of granular assemblies for 3 loading/unloading cycles performed in [19] for experimental measurement of k_{eff}. Hence, the fourth loading cycle is considered for the effective thermal conductivity calculations in later sections of this paper.

The effective thermal conductivity of a granular assembly depends on the microstructural parameters as mentioned before. Typically, the microstructural parameters are obtained from the DEM simulations discussed in this section. Hence, the calculation of k_{eff} through the analytical model presented in this paper still requires computationally intensive DEM simulations for the estimation of the microstructural parameters. In order to eliminate the time consuming DEM simulations to predict the microstructural parameters, a set of parametric correlations are presented in the following.

3.2 Parametric correlations for the microstructural parameters

The initial packing fraction (η_0: packing fraction of the assembly at the end of the third cycle) can be controlled through the DEM simulations. The RCP algorithm can generate assemblies with required packing fractions (η_{RCP}) which are then compressed for three loading/unloading cycles to get the desired initial packing fraction (η_0). Thus, the initial packing fraction (η_0) and the compression state (macroscopic strain along the axial direction) can be controlled in the DEM simulations for obtaining the required configuration of the assembly. This results in a unique

Fig. 11 a Effective thermal conductivity as a function of instantaneous packing fraction (η) for different initial packing fractions (η_0), **b** Correlation for instantaneous packing fraction η with the normalized macroscopic stress σ_{zz}/E for different initial packing fractions η_0

(a)

(b)
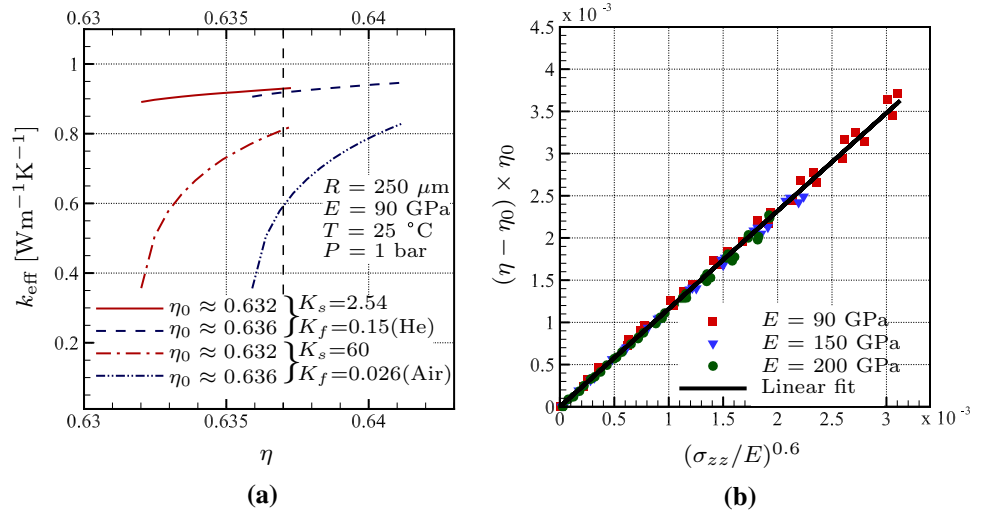
assembly for every η_0 and compression state. For example, consider an instantaneous packing fraction $\eta = 0.637$ (dashed vertical line in Fig. 11a) which can be achieved by

1. Compressing an assembly with $\eta_0 = 0.636$ to a certain compression state or
2. Compressing an assembly with $\eta_0 = 0.632$ to a higher compression state than the above.

The above two methods results in different configurations even though the final packing fraction of the assemblies is the same. Since, the assembly with $\eta_0 = 0.636$ undergoes less strain than the assembly with $\eta_0 = 0.632$ to reach equal final packing fraction η, the assembly with $\eta_0 = 0.636$ will have less contacts than the one with $\eta_0 = 0.632$. Hence, the resulting effective thermal conductivity for the assembly with $\eta_0 = 0.636$ will be less than the assembly with $\eta_0 = 0.632$, even with the equal values of η as shown in Fig. 11a. Further, for the beds with high solid to gas conductivity ratio (K_s/K_f), the difference in k_{eff} is higher than that for the bed with lower solid to gas conductivity ratio. Also, it can be noticed that the increase in k_{eff} with increase in compression is higher for the beds with high solid to gas conductivity ratio. Also, the nature of increase of k_{eff} with η indicates that the k_{eff} might reach saturation as the η increases with increasing loading as the assembly gets jammed. A similar effect of the state of compression on k_{eff} for different solid to gas conductivity ratios was also observed experimentally [12, 17, 19]. Thus, it can be concluded that the effective conductivity of a granular bed is not just a function of the packing fraction, but also depends on the state of compression. The analytical estimation of k_{eff} requires the specification of microstructural parameters. These microstructural parameters in turn depend on the compression history of the assembly. In this work, we use macroscopic stress along the axial direction (σ_{zz}) for quantifying the compression state (history of bed). In the following, correlations

are developed for microstructural parameters as a function of the initial packing fraction (η_0) and the macroscopic stress (σ_{zz}) normalized with Young's modulus of the pebble material (E). The values of 90–200 GPa, 0.25 and 0.1 are taken for the Young's modulus, Poisson's ratio and the friction coefficient for the DEM simulations. Since, the effective conductivity almost saturates after fourth cycle, the fourth loading cycle is used for the estimation of microstructural parameters.

The values of microstructural parameters corresponding to the fourth loading cycle of all four RCP packing fractions ($\eta_{RCP} \approx 0.61, 0.62, 0.63$ and 0.64) are plotted for each Young's modulus ($E = 90, 150$ and 200 GPa) in the Figs. 11b, 12a and 13. Figure 11b shows the increase in packing fraction with normalized macroscopic stress (σ_{zz}/E) as the assembly is compressed. Figure 12a shows the variation of total coordination number (N) with initial packing fraction (η_0). The total coordination number N is the sum of the coordination numbers N_o and N_g. The total coordination number (N) in Fig. 12a corresponds to the uncompressed assembly after 3 full cycles. It was observed in the current work and also in literature [6] that the total coordination number N is almost constant with compression and also cyclic loading (see Sect. 3.1). Hence, the total coordination number (N) is taken to be constant with stress (σ_{zz}) for a given η_0. Figure 12b shows the variation of the overlap coordination number (N_o) with the normalized macroscopic stress (σ_{zz}/E). Different correlations are reported in the literature [22, 32] for the overlap coordination number in terms of instantaneous packing fraction (η) without the consideration of history of the bed. Now, the gap coordination number (N_g) can be obtained by subtracting N_o from the total coordination number (N). Figure 13a shows the variation of normalized mean contact radius ($\bar{r}_c/R$) with normalized stress (σ_{zz}/E). It was observed that the normalized mean contact radius ($\bar{r}_c/R$) varies linearly with $(\sigma_{zz}/E)^{1/3}$. A similar result was also observed in [53] in terms of normalized average

Fig. 12 **a** Correlation for total coordination number N with the initial packing fraction (η_0), **b** Correlation for the overlap coordination number N_o with the normalized macroscopic stress σ_{zz}/E for different η_0

(a)

(b)
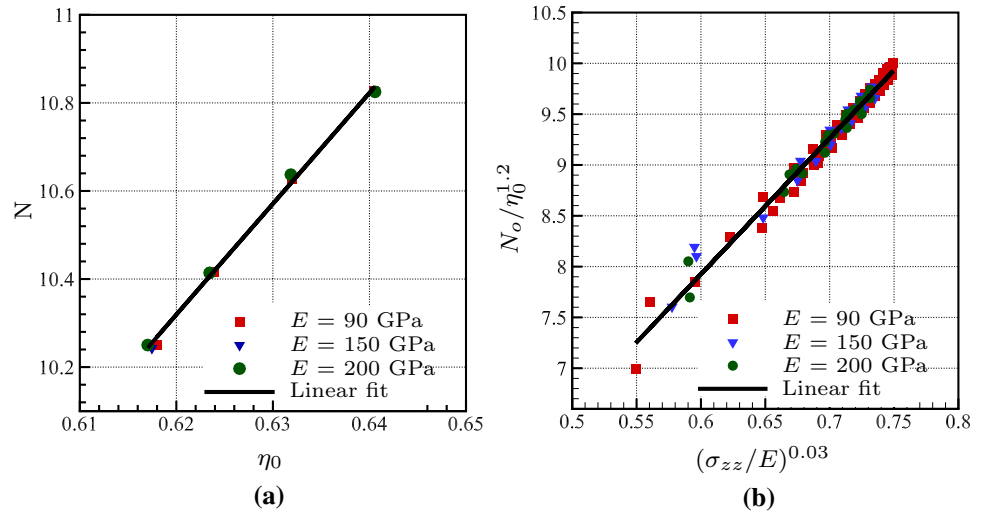
Fig. 13 Correlation for the **a** mean contact radius $\bar{r}_c$, **b** effective gap h_e with the normalized macroscopic stress σ_{zz}/E for different η_0

(a)

(b)
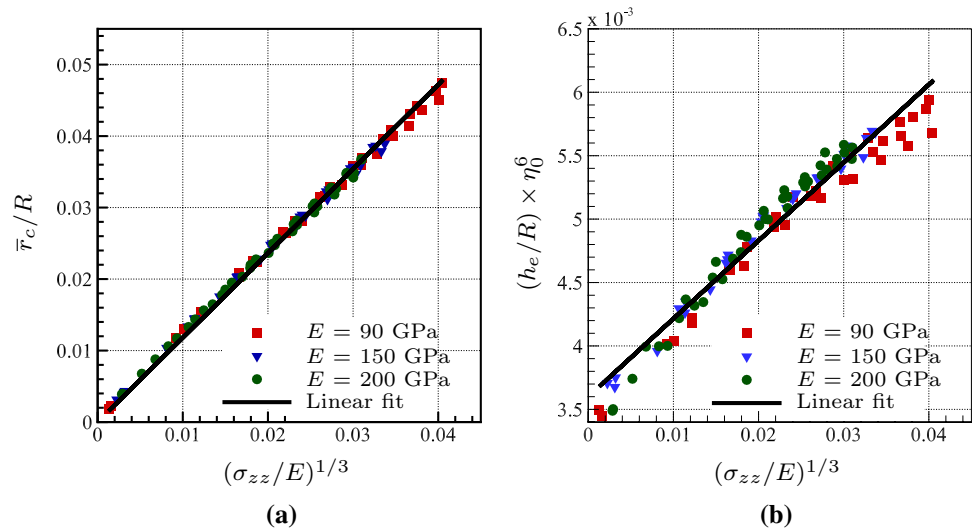
normal contact force as a function of hydrostatic stress independent of η_0. Figure 13b shows the variation of normalized effective gap (h_e/R) with the increasing normalized stress (σ_{zz}/E). The MATLAB Curve Fitting Toolbox™is used in estimating the best linear fits of the microstructural parameters. The parametric correlations attained in this section for estimating the microstructural information from the experimentally available parameters (η_0, R, σ_{zz} and E) are as follows.

$$\eta = 1.16 \times (\sigma_{zz}/E)^{0.6}/\eta_0 + \eta_0$$
$$N = 25.16 \times \eta_0 - 5.28$$
$$N_o = \eta_0^{1.2} \times (13.39 \times (\sigma_{zz}/E)^{0.03} - 0.1093)$$
$$N_g = N - N_o \tag{3.2}$$
$$\bar{r}_c = R \times (1.18 \times (\sigma_{zz}/E)^{1/3})$$
$$h_e = R \times (0.0615 \times (\sigma_{zz}/E)^{1/3} + 0.0036)/\eta_0^6$$

The RCP algorithm generates granular assemblies with least possible number of contacts (in most cases only 1 overlap contact will be there). Hence, for obtaining the microstructural parameters for a realistic uncompressed assembly through our model, the assemblies generated from RCP are compressed to a small value of macroscopic stress ($= 100$ Pa). These parametric correlations are validated by comparing the values of k_{eff} estimated using the microstructural parameters obtained as above with that of the numerical model presented in Sect. 2.1.

3.3 Validation of parametric correlations

The parametric correlations are validated with new assembly configurations generated by compressing the assemblies with $\eta_0 = 0.636$. Note that, these assemblies are not used for estimating the correlations given in
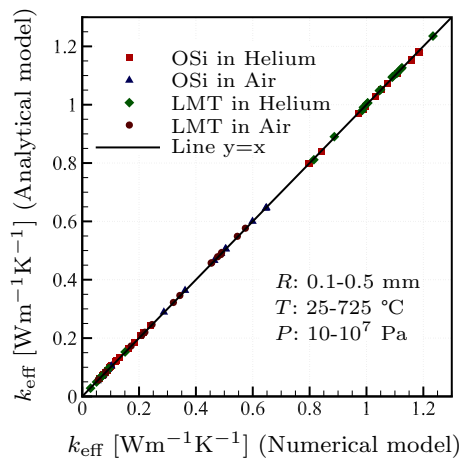
Fig. 14 Comparison of k_{eff} evaluated from the numerical model with that of k_{eff} calculated from the analytical model with microstructural parameters estimated from the parametric correlations for different granular assembly parameters

Eq. 3.2. Figure 14 shows the comparison of the effective thermal conductivities calculated by the numerical model and the analytical model by employing the above identified parametric correlations to represent the microstructural information instead of importing the specific microstructural data of the respective assembly. Compressed assemblies are considered with $\eta_0 = 0.636$ using the material properties of Lithium Orthosilicate (OSi), Lithium Metatitanate (LMT) granules in Helium/Air environment. The material properties are presented in Table 1. A good

agreement is observed between the effective conductivities estimated by the numerical model and the analytical model using parametric correlations for determining microstructural parameters. Thus, the dependence on the DEM simulations for the analytical estimation of k_{eff} is now eliminated with the assistance of parametric correlations without loss in accuracy. The analytical model for k_{eff} with microstructural parameters estimated from the parametric correlations will be refereed to as the analytical model in later sections.

4 Results and discussion

In this section, the effective thermal conductivity of granular beds evaluated from the analytical model is compared with the experimental measurements reported in the literature [10–17, 19, 20]. Figures 15, 16, 17 and 18 show the comparison of the analytical k_{eff} with the experimental measurements for various granular systems. The experimental results of k_{eff} for granular beds are divided into two parts—low and high solid to gas conductivity ratios to address the range of values for the fitting parameter ζ for each case. To show the effect of fitting parameter ζ on k_{eff}, a comparison of the analytical k_{eff} with the experiments for different values of ζ is presented later in this section (Figs. 15a, 17c). As the analytical model is developed for monosized granular beds, the mean diameter is considered as the diameter of granules for the evaluation of k_{eff} for polydisperse granular beds. Since, the numerical and analytical models are in good agreement,

Table 1 Bulk properties of Lithium ceramic granules, Helium and Air

Material	Property		Numerical value
OSi	K_s	W m^{-1} K^{-1}	$-1.596 \times 10^{-9}T^3 + 3.042 \times 10^{-6}T^2 - 0.0019T + 2.591$, T in °C [56]
			$(1.98 + 850/T)(1-p)/(1 + p(1.95 - 8 \times 10^{-4}T))$, $p \approx 0.05$, T in K [57]
	E	GPa	90
	m_s	g mol^{-1}	119.85
LMT	K_s	W m^{-1} K^{-1}	$[(1-p)/(1 + (1.06 - 2.88 \times 10^{-4}T)p)](4.77 - 5.11 \times 10^{-3}T + 3.12 \times 10^{-6}T^2)$, $p \approx 0.08$, T in K [58]
			$(1-p)^{2.9}(5.35 - 4.78 \times 10^{-3}T + 2.87 \times 10^{-6}T^2)$, $p \approx 0.08$, T in K [59]
	E	GPa	200.6
	m_s	g mol^{-1}	109.76
LZT	K_s	W m^{-1} K^{-1}	$(1-p)^{(5/3)}(3.643/(1 + 0.00155T) + 7.579 \times 10^{-10}T^3)$, $p \approx 0.2$, T in K [60]
	E	GPa	70
	m_s	g mol^{-1}	153.1
Helium	K_f	W m^{-1} K^{-1}	$3.366 \times 10^{-3}T^{0.668}$, T in K [61]
	ν	μPa s	$18.65 \times (T/273.16)^{0.7}$, T in K [62]
	m_f	g mol^{-1}	4
Air	K_f	W m^{-1} K^{-1}	$-8.652 \times 10^{-9} T^2 + 7.038 \times 10^{-5} T + 0.006237$, T in K [63]
	ν	μPa s	$-1.674 \times 10^{-5}T^2 + 0.05805 \times T + 2.134$, T in K [63]
	m_f	g mol^{-1}	28.96

Fig. 15 Comparison of k_{eff} estimated using the analytical model with different experimental measurements for OSi granular beds in the presence of stagnant gas Helium/Air [15, 19]: **a** comparison of k_{eff} estimated from the analytical model with different values for fitting parameter (ζ) with the experimental measurements of k_{eff} for a granular bed with low solid to gas conductivity ratio (Osi in Helium/Air), **b** effect of the macroscopic stress (σ_{zz}) on k_{eff} for OSi bed in Helium, **c** effect of the gas pressure on k_{eff} for OSi bed in Helium/Air, compared with k_{eff} from analytical model with and without including the contribution of radiation to effective conductivity, **d** effect of gas pressure on k_{eff} for OSi beds in Helium/Air showing the characteristic S-curve of Smoluchowski effect. (In the figures, E refers to the experimental measurements, whereas, A refers to the predictions of the proposed analytical model)
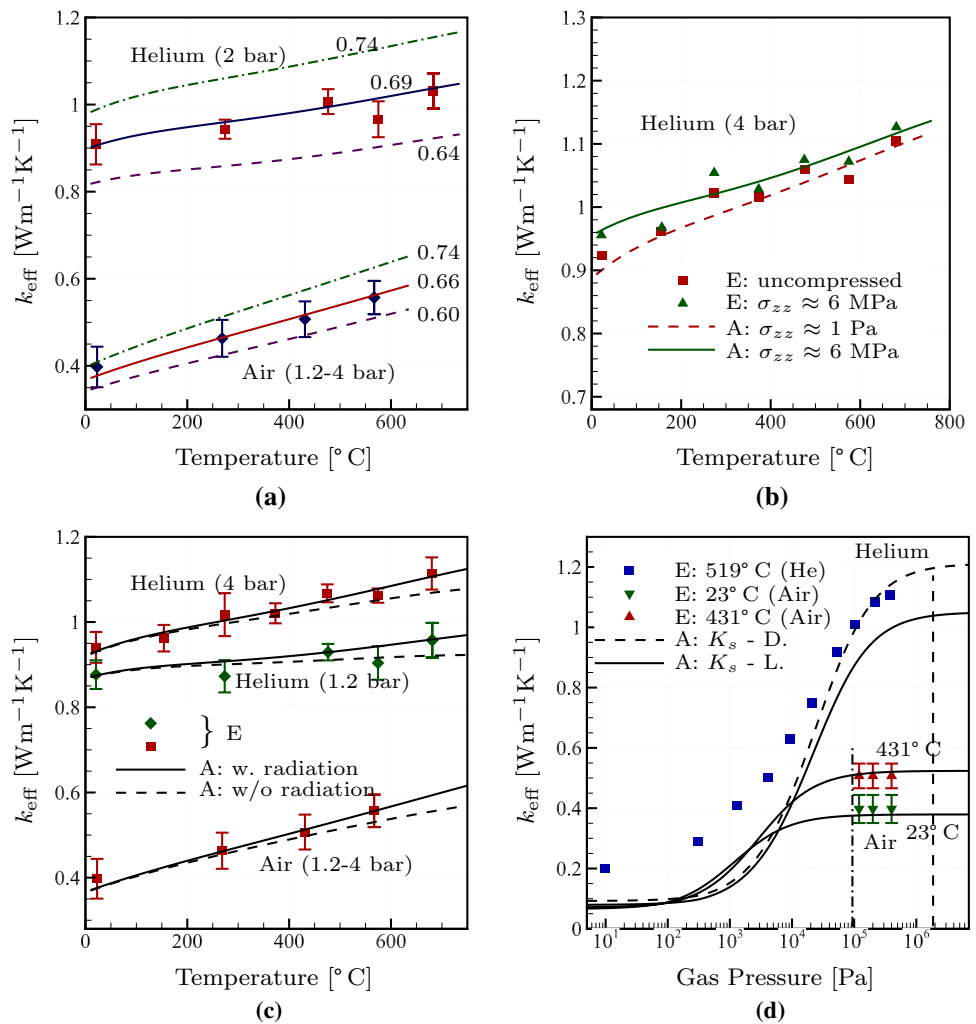
Fig. 16 Experimental k_{eff} compared with the analytical k_{eff} with and without including the contribution of radiation to the effective conductivity, **a** 1: 1 mm LMT granules with a packing fraction of 63% in Helium [20] and 2: 1.9 mm LMT granules with a packing fraction of 60% in Helium [16], **b** 1.2 mm LZT granules in Helium [13]. (In the figures, E refers to the experimental measurements, whereas, A refers to the predictions of the proposed analytical model)
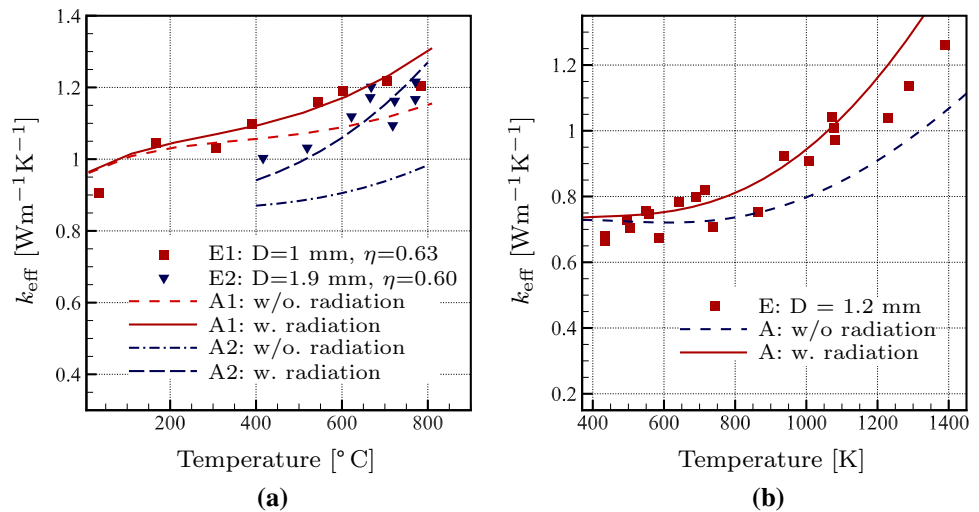

only the analytical model is compared with the experiments in this section. Also, note that the contribution of radiation to k_{eff} is considered as per Sect. 2.6 in the analytical k_{eff} unless otherwise stated.

4.1 Low solid to gas conductivity ratio

A solid to gas conductivity ratio less than 500 is considered as low in this work. The values of the fitting parameter ζ

Fig. 17 Comparison of k_{eff} estimated using the analytical model with different experimental measurements: Effect of the gas pressure on k_{eff} for **a** LZT granular beds in presence of stagnant Helium [13] for different bed temperatures, **b** Alumina [14], Magnesium Oxide [10] and Uranium [11] granular beds in presence of stagnant Helium. **c** Comparison of k_{eff} estimated from the analytical model with different values for fitting parameter (ζ) with the experimental measurements of k_{eff} for a granular bed with high solid to gas conductivity ratio (Uranium in Argon [11]). **d** Effect of the size of particles on k_{eff} and the saturation pressure for Uranium granules in Nitrogen [11]. (In the figures, E refers to the experimental measurements, whereas, A refers to the predictions of the proposed analytical model)
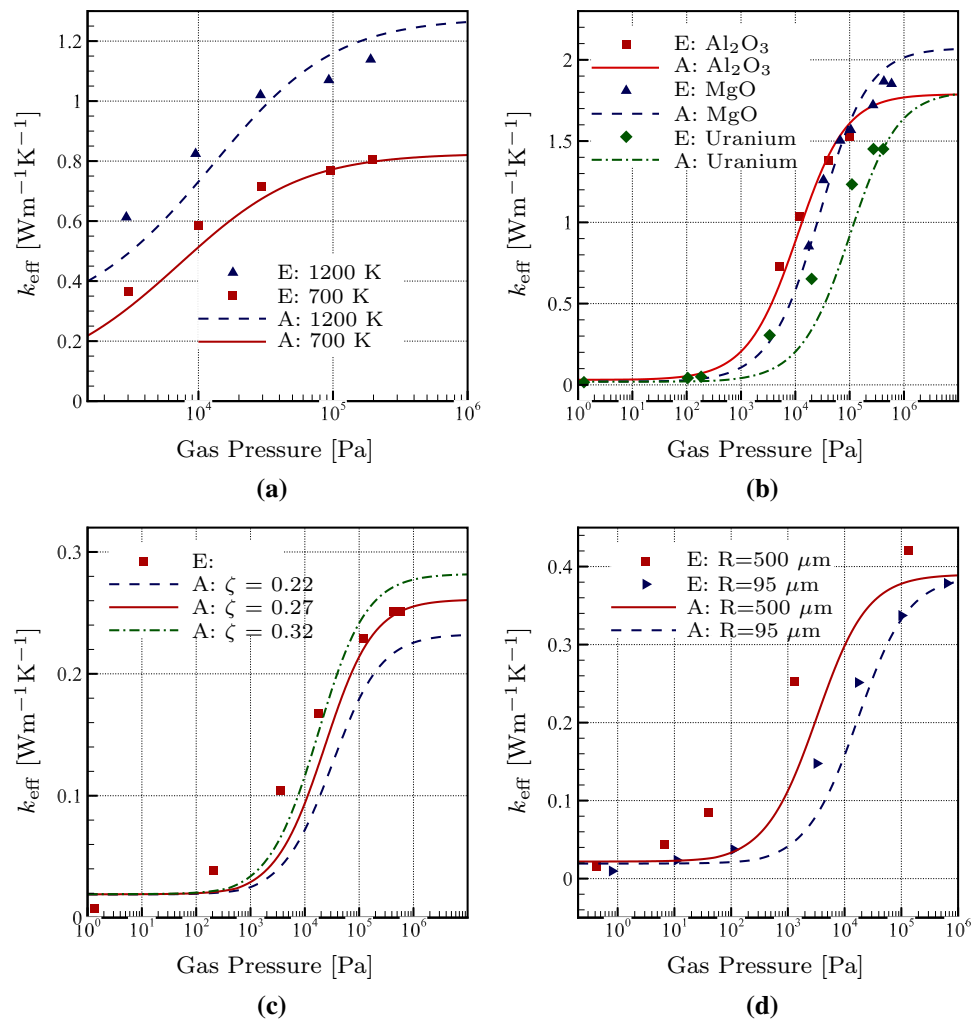
is found to lie in the range of 0.5–0.75 for assemblies with solid to gas conductivity ratios less than 500. The solid to gas conductivity ratio lies in the range of 5–100 for the Lithium ceramic granules [Lithium Orthosilicate(OSi), Lithium Metatitanate (LMT) and Lithium Metazirconate (LZT)] in the presence of Helium/Air.

4.1.1 Lithium orthosilicate granules in Helium/Air

Pupeschi et al. [19] reported the experimental measurements of k_{eff} for polydisperse OSi granules in Helium/Air at different gas pressures and bed temperatures. The OSi beds have undergone mechanical conditioning of 3 full loading/unloading cycles before measuring the effective thermal conductivity. The reported values of k_{eff} for the OSi granular bed are mean values of the k_{eff} measured at 0 and 6 MPa uni-axial stress. As the current analytical model is developed for monosized pebble beds, we use the mean diameter of the bed as the diameter (360 μm). The packing fraction of the uncompressed bed is reported as 0.642. Thus, the inputs for the estimation of the microstructural parameters (η, N_o, N_g, $\bar{r}_c$,

h_e) from the parametric correlations are taken as $\eta_0 = 0.642$, $D = 360$ μm and $E = 90$ GPa. The bulk conductivity of OSi granules is determined by means of the polynomial fit for the conductivity values reported in [56]. The other material properties are mentioned in Table 1. The fitting parameter ζ is determined through trial and error in the range of 0.5–0.75 to best fit with experimental observations. Figure 15a shows the comparison of k_{eff} estimated from the analytical model with experiments for different values of fitting parameter ζ. It can observed that the analytical model fits better with experimental results for Helium with $\zeta=0.69$, whereas, $\zeta = 0.66$ fits better for Air. This lower value of ζ for the case of Air than ζ for the case of Helium might be due to higher solid to gas conductivity ratio of Air ($35 < \alpha_0 < 100$) than that of Helium ($5 < \alpha_0 < 20$). Also, it was observed that $\zeta = 0.69$ gives good agreement with experimental measurements of k_{eff} for all other Lithium ceramic granules in Helium. Hence, a value of 0.69 for ζ is used in this work for all Lithium ceramic granules in Helium. It is observed from both experimental and analytical results in Fig. 15b, that k_{eff} varies slightly with compression for the OSi bed in Helium.

The analytical k_{eff} reported in this section for the OSi beds is the mean of the effective conductivities for $\sigma_{zz} = 1$ Pa and 6 MPa unless mentioned otherwise. Figure 15c shows k_{eff} evaluated from the analytical model with and without the effect of radiation at different gas pressures (1.2 and 4 bar). The contribution of the radiation to k_{eff} is observed to be small for this 0.36 mm granules for a temperature range of 20–700 °C. This is in accordance with the findings of Asakuma et al. [48], that the contribution of radiation to k_{eff} is negligible for granular beds with temperatures less than 1000 K and particle diameters less than 1 mm.

Enoeda et al. [15] reported the effective conductivity for OSi bed in Helium over wider range of gas pressures (1–10^6 Pascals). The bed parameters for the OSi bed reported in [15] are $\eta = 0.625$, D = 0.44 mm. Different bulk conductivity values for OSi particles are reported in the literature [34, 56, 57]. The analytical model with K_s from Donne and Sordon [57] (denoted as $K_s - D$) matches better with experiments compared to K_s from Löbbecke et al. [56] (denoted as $K_s - L$) as observed in Fig. 15d. This may be due to the difference in the materials and other uncertainties in the experimental conditions. The analytical model is able to capture the characteristic S-curve of the Smoluchowski effect (Fig. 15d). At low pressures, the experimental k_{eff} is higher than the analytical model predictions. This error might be due to uncertainties in the experiments since, k_{eff} as high as 0.2 W m^{-1} K^{-1} at almost vaccum (10 Pa gas pressure) for an uncompressed OSi bed is not expected. Even for Uranium granules with bulk conductivity almost 10 times higher than OSi, k_{eff} reported experimentally is only 0.05 W m^{-1} K^{-1} at 10 Pa gas pressure (see Fig. 17b).

From Fig. 15d, it is observed that the saturation pressure for Helium is higher than that of Air resulting in the S-curve for the case of Helium to be on the right of that of Air. This is due to the higher mean free path for Helium than for Air at a given state leading to higher Knudsen number (K_n). This results in a lower saturation pressure for Air than for Helium. Furthermore, from the S-curves of a bed in Air at different temperatures, it is observed that the saturation pressure depends on the temperature of the bed. This behavior is the consequence of dependence of the mean free path on the temperature. From the comparison to experiments presented above, it can be concluded that the analytical model is able to capture the effect of stress, temperature, gas pressure and the nature of gas on the effective thermal conductivity of OSi granular beds.

4.1.2 Lithium metatitanate granules in Helium

The experimental results presented by Panchal et al. [20] and Hatano et al. [16] are compared with the analytical model for Lithium Metatitanate (LMT) granules. Panchal et al.

[20] performed experiments with uncompressed bed at a packing fraction of 63% (achieved through vibrations) of 1 mm diameter LMT granules in Helium. Hatano et al. [16] performed experiments with uncompressed bed at a packing fraction of 60% of 1.9 mm diameter LMT granules in Helium. For the analytical estimation of k_{eff}, we considered the microstructural parameters corresponding to $\eta_0 = 0.63$ with 1 mm sized granules and $\eta_0 = 0.60$ with 1.9 mm sized granules. The stress state is assumed to be $\sigma_{zz} = 100$ Pa. Different bulk conductivity values (K_s) are reported in the literature [58, 59] for LMT granules. The material properties can be seen in Table 1. Figure 16a shows the comparison of k_{eff} from the experiments with k_{eff} as predicted by the analytical model with and without including the effect of radiation. The analytical model with K_s from [58] matches with experimental values of k_{eff} reported in Hatano et al. [16], whereas, K_s from [59] matches with experimental values of k_{eff} reported in Panchal et al. [20]. It is observed from the Fig. 16a that k_{eff} from the analytical model with the inclusion of radiation matches best with the experiments. Also, it can be noticed that the effect of radiation predicted by the analytical model is higher for 1.9 mm granules than the 1 mm granules (according to Eq. 2.21).

4.1.3 Lithium metazirconate granules in Helium

The experimental results presented at [13] on Lithium Metazirconate beds in Helium are compared with the analytical model predictions. The input parameters for the analytical model such as temperature, gas pressure, packing fraction and particle size are taken from the experiments [13]. A nominal macroscopic stress (σ_{zz}) of 100 Pa is considered for the estimation of the microstructural parameters. A wide range of bulk conductivity values are reported for LZT in the literature [64]. The design correlation for K_s of LZT as reported by the International Thermonuclear Experimental Reactor (ITER) team is used in this work [60]. The material properties are mentioned in Table 1. The comparison of k_{eff} from the analytical model with the experimental results for LZT bed with different temperatures [13] is presented in Fig. 16b. It can be noticed that the k_{eff} from analytical model with inclusion of radiation is in good agreement with the experimental results. At low temperatures, the contribution of radiation to k_{eff} is negligible. However, at high temperatures, k_{eff} with and without the effect of radiation diverge as observed in Fig. 16b. This significant difference is because of the size of the particles (1.2 mm) as the radiative heat transfer is proportional to particle size (according to Eq. 2.21). Figure 17a shows the comparison of the analytical model including the contribution of radiation with the experimental results [13] demonstrating the effect of the gas pressure on k_{eff}. It can be noticed from the Figs. 16b and 17a

that the analytical model is able to predict the experimental results with a reasonable accuracy for LZT granular beds.

4.1.4 Some other assemblies with low solid to gas conductivity ratio

Figure 17b shows the comparison of k_{eff} from the analytical model with experimental measurements for Alumina [14], Magnesium oxide [10] and Uranium granules [11] in the presence of Helium. The input parameters for the analytical model such as packing fraction, particle size, temperature and gas pressures are same as the experimental conditions. The stress state is considered as $\sigma_{zz} = 100$ Pa for the three assemblies. The fitting parameter ζ is determined through trial and error to best fit with experimental observations similar to the case of Lithium ceramics mentioned before. The input parameters (η_0, R, E) used for estimating the microstrcutural parameters are as shown in Table 2. Furthermore, Table 2 shows the bulk conductivity of the granules, the corresponding solid to gas conductivity ratios and the values of ζ taken for each assembly. The bulk conductivity of Helium is estimated as a function of temperature as given in Table 1. A satisfactory agreement is observed between the analytical and experimental results as shown in Fig. 17b.

4.2 High solid to gas conductivity ratio

A solid to gas conductivity ratio greater than 500 is considered as high in this work. For such assemblies, the fitting parameter (ζ) lies in the range of 0.1–0.5. For validating the analytical model at high solid to gas conductivity ratios, k_{eff} from the analytical model is compared with different granular assemblies (Beryllium in Helium [12], Uranium in Nitrogen/Argon [11], Steel in Air [17]). The input parameters (η_0, R, E) used for estimating the microstrcutural parameters are as shown in Table 3. Furthermore, Table 3 shows the bulk conductivity of the granules and the corresponding solid to

gas conductivity ratios taken for each assembly. The bulk conductivity and viscosity values of Helium and Air are estimated as per correlations presented in Table 1. The conductivities of Argon and Nitrogen at the room temperature are taken as 0.0177 W m^{-1} K^{-1} and 0.0257 W m^{-1} K^{-1}, respectively [65]. The viscosity values of Argon and Nitrogen at the room temperature are taken as 22.9 µPa s and 17.8 µPa s, respectively [65]. For the Uranium in Nitrogen/Argon beds, macroscopic stress $\sigma_{zz} = 100$ Pa is used. Figure 17c shows the comparison of k_{eff} estimated from the analytical model with experimental measurements for Uranium in Argon with different values for fitting parameter ζ. It can observed that a value of 0.27 for ζ fits the experimental measurements better. Similarly, the values of ζ are determined for other assemblies and presented in Table 3.

Figure 18a, b show the effect of stress on k_{eff} for beds with high solid to gas conductivity ratios. It is observed that for the assemblies with high solid to gas conductivity ratio (Be in Helium and Steel in Air), the effect of σ_{zz} is significant in contrast to what we observed for the case of low solid to gas conductivity ratio (OSi in Helium) assemblies. This is because, in the case of beds with high solid to gas conductivity ratio, the solid conduction contributes most to the effective conductivity. This solid conduction occurs through overlap contact area which scales with the stress on the bed. Figure 17d shows the comparison of analytical and experimental k_{eff} for Uranium granular assemblies with different mean sizes of granules in stagnant Nitrogen. For both sizes, the same value of ζ is used. The saturation pressure as predicted by the analytical model is lower for the larger particles than the smaller particles as observed in the Fig. 17d for the same gas type and temperature. This is due to the dependence of the Knudsen number on the characteristic dimension of the contacts which depends on the particle sizes.

Note that the effective conductivity is estimated by the analytical model using directly experimentally available

Table 2 Parameters used for estimating k_{eff} of granular assemblies presented in Fig. 17b

Materials	η	R (µm)	E (GPa)	T (°C)	K_s (W m^{-1} K^{-1})	α_0	ζ
Al$_2$O$_3$ in He	0.567	500	215	300	14.4	60.8	0.66
MgO in He	0.58	100	250	200	30	150	0.6
Uranium in He	0.6	95	200	25	28	185	0.6

Table 3 Parameters used for estimating k_{eff} for different granular assemblies

Materials	η	R (µm)	E (GPa)	T (°C)	P ($\times 10^5$) (Pa)	K_s (W m^{-1} K^{-1})	α_0	ζ
Beryllium in He (Fig. 18a)	0.56	1000	300	33	0.93	150	973.6	0.36
Uranium in N$_2$ (Fig. 17d)	0.6	–	200	25	–	28	1089.5	0.36
Uranium in Ar (Fig. 17c)	0.6	95	200	25	–	28	1581.9	0.27
Steel in Air (Fig. 18b)	0.56	250	200	33	1	73	2706.5	0.14

Fig. 18 Comparison of k_{eff} estimated using the analytical model with different experimental measurements: Effect of the macroscopic stress (σ_{zz}) on k_{eff} for assemblies composed of **a** Beryllium granules in Helium [12], **b** steel granules in Air [17]. (In the figures, E refers to the experimental measurements, whereas, A refers to the predictions of the proposed analytical model)
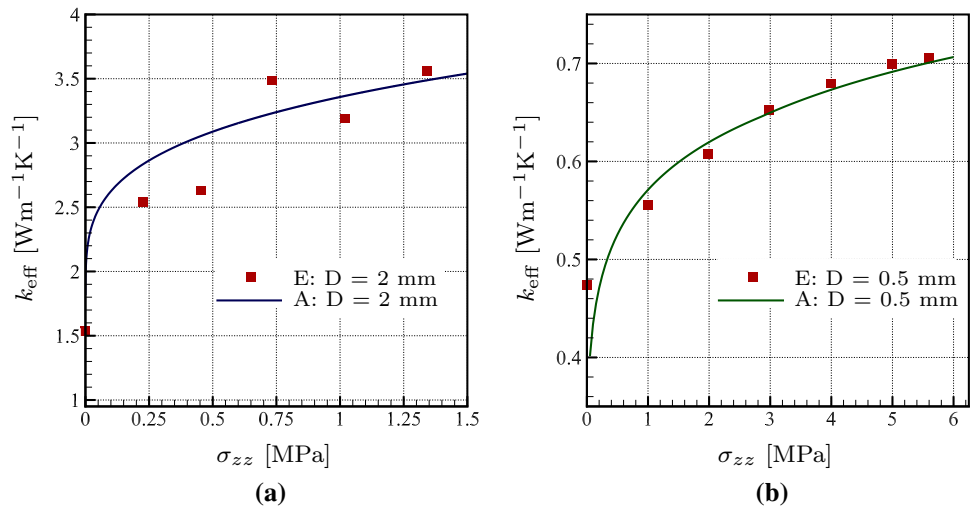
parameters (such as bed properties like initial packing fraction η_0, macroscopic stress σ_{zz}, temperature T, gas pressure P, particle diameter D and bulk properties of solid like thermal conductivity K_s, molecular weight m_s, Young's modulus E and bulk properties of interstitial gas like thermal conductivity K_f, molecular weight m_f, viscosity of gas v) without any dependence on simulations. The analytical model proposed in this paper includes the effect of the microstructural parameters of a bed, radiation and the Smoluchowski effect in the estimation of k_{eff} resulting in a good agreement between the experiments and the analytical model. The effect of gas type, particle size, temperature on the saturation pressure for the k_{eff} is captured satisfactorily. The value of the fitting parameter (ζ) is selected to best match the analytical predictions with the experimental results based on the value of solid to gas conductivity ratio (α_0). However, a relation between ζ and α_0 currently doesn't exist which may be established in future work, so as to decipher a physical significance to the parameter ζ.

5 Summary and conclusions

An analytical model including the Smoluchowski effect and the effect of heat flow through radiation for the estimation of the effective thermal conductivity of a monosized granular assembly in the presence of a stagnant gas is presented. The analytical model presented in this work depends on the microstructural parameters (instantaneous packing fraction η, total coordination number N, overlap coordination number N_o, gap coordination number N_g, mean contact radius $\bar{r}_c$, effective gap h_e) of the assembly as well as the bulk material properties of the granules and the surrounding gaseous medium. For the numerical estimation of k_{eff}, a modified Resistor Network model with the inclusion of Smoluchowski effect has been developed. In a granular assembly, the gas is

confined in small gaps leading to a reduction in conductivity of the gas with decreasing gas pressure. This dependence of the gas conductivity at each contact on the gas pressure is estimated in terms of Knudsen number. The mean free path of the gas molecules needed to estimate the Knudsen number is calculated based on the relationship between viscosity and mean free path. A simplified estimate of the contribution of radiation to the effective conductivity is evaluated in terms of the emissivity of the surface of the particles and the temperature of the assembly.

A numerical investigation on the effect of compressive cyclic loading on the microstructural parameters is carried out. The microstructural parameters showed saturation with the increasing number of loading/unloading cycles indicating that the major local rearrangements are limited to few initial cycles. The effective thermal conductivity of the bed is not only a function of instantaneous packing fraction but also depends on the history of the bed which can be quantified by the initial packing fraction and the macroscopic compression state. The difference in k_{eff} of assemblies with same instantaneous packing fractions, but different histories is proportional to the solid to gas conductivity ratio. The increase in k_{eff} of an assembly with an increase in compression is proportional to it's solid to gas conductivity ratio. Parametric correlations to estimate the microstructural parameters (η, N, N_o, N_g, $\bar{r}_c$, h_e) from the experimentally known initial packing fraction η_0, macroscopic stress along the axial direction σ_{zz} and Young's modulus of the solid material E have been obtained in the form of empirical relations. The dependency of the analytical model on DEM simulations to obtain the microstructural parameters is thus eliminated with the help of parametric correlations. The contribution of radiation to the effective conductivity is significant only for beds with particle sizes greater than 1 mm and bed temperatures more than 1000 K. The effective thermal conductivity estimated from the analytical model

using the parametric correlations is in good agreement with the numerical as well as the experimental results for different granular assemblies reported in the literature. The value of the fitting parameter (ζ) is inversely related to the solid to gas conductivity ratio of a granular assembly. The fitting parameter lies in the range of 0.5–0.75 for low solid to gas conductivity ratios, whereas, for high solid to gas conductivity ratios it falls in the range of 0.1–0.5. The proposed analytical model is able to predict the experimental measurements of k_{eff} of a granular assembly fairly well over a wide range of solid to gas conductivity ratios (10–2500), gas pressures (10–10^6 Pa), bed temperatures (25–1000 °C), particle diameters (0.2–2 mm) and packing fractions (0.56–0.65).

Compliance with ethical standards

Conflict of interest The authors declare that they have no conflict of interest.

References

1. van der Laan, J.G., Reimann, J., Fedorov, A.V.: Ceramic breeder materials. In: Reference Module in Materials Science and Materials Engineering, pp. 1–63. Elsevier (2016). https://doi.org/10.1016/B978-0-12-803581-8.00733-5 (ISBN 978-0-12-803581-8)

2. Ying, A., Reimann, J., Boccaccini, L., Enoeda, M., Kamlah, M., Knitter, R., Gan, Y., van der Laan, J.G., Magielsen, L., Maio, P.D., Dell'Orco, G., Annabattula, R.K., Lew, J.T.V., Tanigawa, H., van Til, S.: Status of ceramic breeder pebble bed thermo-mechanics R&D and impact on breeder material mechanical strength. Fusion Eng. Des. **87**(7), 1130–1137 (2012)

3. Fogler, H.S., et al.: Elements of Chemical Reaction Engineering. Prentice-Hall International, London (1999)

4. Farid, M., Khudhair, A., Razack, S., Al-Hallaj, S.: A review on phase change energy storage: materials and applications. Energy Convers. Manag. **45**(9–10), 1597–1615 (2004)

5. Singhal, S.: Advances in solid oxide fuel cell technology. Solid State Ion. **135**(1), 305–313 (2000)

6. Peeketi, A.R., Moscardini, M., Vijayan, A., Gan, Y., Kamlah, M., Annabattula, R.K.: Effective thermal conductivity of a compacted pebble bed in a stagnant gaseous environment: An analytical approach together with DEM. Fusion Eng. Des. **130**, 80–88 (2018)

7. Gan, J., Zhou, Z., Yu, A.: Effect of particle shape and size on effective thermal conductivity of packed beds. Powder Technol. **311**, 157–166 (2017)

8. Moscardini, M., Gan, Y., Pupeschi, S., Kamlah, M.: Discrete element method for effective thermal conductivity of packed pebbles accounting for the Smoluchowski effect. Fusion Eng. Des. **127**, 192–201 (2018)

9. Hou, Q.F., Zhou, Z.Y., Yu, A.B.: Computational study of the effects of material properties on heat transfer in gas fluidization. Ind. Eng. Chem. Res. **51**(35), 11,572–11,586 (2012)

10. Diessler, R., Boegli, J.: An investigation of effective thermal conductivities of powders in various gases. Trans. ASME **80**, 1417–1425 (1958)

11. Swift, D.L.: The thermal conductivity of spherical metal powders including the effect of an oxide coating. Int. J. Heat Mass Transf. **9**(10), 1061–1074 (1966)

12. Tehranian, F., Abdou, M.A.: Experimental study of the effect of external pressure on particle bed effective thermal properties. Fusion Technol. **27**(3), 298–313 (1995)

13. Earnshaw, J.W., Londry, F.A., Gierszewski, P.J.: The effective thermal conductivity of a bed of 1.2-mm-diam lithium zirconate spheres in helium. Fusion Technol. **33**(1), 31–37 (1998)

14. Slavin, A.J., Londry, F.A., Harrison, J.: A new model for the effective thermal conductivity of packed beds of solid spheroids: alumina in helium between 100 and 500°C. Int. J. Heat Mass Transf. **43**(12), 2059–2073 (2000)

15. Enoeda, M., Ohara, Y., Roux, N., Ying, A., Pizza, G., Malang, S.: Effective thermal conductivity measurement of the candidate ceramic breeder pebble beds by the hot wire method. Fusion Technol. **39**(2P2), 612–616 (2001)

16. Hatano, T., Enoeda, M., Suzuki, S., Kosaku, Y., Akiba, M.: Effective thermal conductivity of a Li_2Tio_3 pebble bed for a demo blanket. Fusion Sci. Technol. **44**(1), 94–98 (2003)

17. Widenfeld, G., Weiss, Y., Kalman, H.: The effect of compression and preconsolidation on the effective thermal conductivity of particulate beds. Powder Technol. **133**(1–3), 15–22 (2003)

18. Yun, T., Dumas, B., Santamarina, J.: Heat transport in granular materials during cyclic fluid flow. Granul. Matter **13**(1), 29–37 (2011)

19. Pupeschi, S., Knitter, R., Kamlah, M.: Effective thermal conductivity of advanced ceramic breeder pebble beds. Fusion Eng. Des. **116**, 73–80 (2017)

20. Panchal, M., Kang, C., Ying, A., Chaudhuri, P.: Experimental measurement and numerical modeling of the effective thermal conductivity of lithium meta-titanate pebble bed. Fusion Eng. Des. **127**, 34–39 (2018)

21. Yun, T.S., Santamarina, J.C.: Fundamental study of thermal conduction in dry soils. Granul. Matter **10**(3), 197 (2008)

22. Van Antwerpen, W., Du Toit, C., Rousseau, P.: A review of correlations to model the packing structure and effective thermal conductivity in packed beds of mono-sized spherical particles. Nucl. Eng. Des. **240**(7), 1803–1818 (2010)

23. Zhou, Z., Yu, A., Zulli, P.: A new computational method for studying heat transfer in fluid bed reactors. Powder Technol. **197**(1–2), 102–110 (2010)

24. Cheng, G., Yu, A., Zulli, P.: Evaluation of effective thermal conductivity from the structure of a packed bed. Chem. Eng. Sci. **54**(19), 4199–4209 (1999)

25. Yun, T.S., Evans, T.M.: Three-dimensional random network model for thermal conductivity in particulate materials. Comput. Geotech. **37**(7), 991–998 (2010)

26. Oschmann, T., Kruggel-Emden, H.: Numerical and experimental investigation of the heat transfer of spherical particles in a packed bed with an implicit 3D finite difference approach. Granul. Matter **19**(3), 47 (2017)

27. Tahmasebi, P., Kamrava, S.: A pore-scale mathematical modeling of fluid-particle interactions: thermo-hydro-mechanical coupling. Int. J. Greenh. Gas Control **83**, 245–255 (2019)

28. Batchelor, G., O'Brien, R.: Thermal or electrical conduction through a granular material. Proc. R. Soc. Lond. Ser. A Math. Phys. Sci. **355**, 313–333 (1977)

29. Argento, C., Bouvard, D.: Modeling the effective thermal conductivity of random packing of spheres through densification. Int. J. Heat Mass Transf. **39**(7), 1343–1350 (1996)

30. Weidenfeld, G., Weiss, Y., Kalman, H.: A theoretical model for effective thermal conductivity (ETC) of particulate beds under compression. Granul. Matter **6**(2–3), 121–129 (2004)

31. Feng, Y., Han, K., Li, C., Owen, D.: Discrete thermal element modelling of heat conduction in particle systems: basic formulations. J. Comput. Phys. **227**(10), 5072–5089 (2008)

32. Kovalev, O., Gusarov, A.: Modeling of granular packed beds, their statistical analyses and evaluation of effective thermal conductivity. Int. J. Thermal Sci. **114**, 327–341 (2017)

33. Martis, J., Annabattula, R.K.: A semi-analytical model for the effective thermal conductivity of a multi-component polydisperse granular bed. Granul. Matter **19**(84), 1–10 (2017)

34. Abou-Sena, A., Ying, A., Abdou, M.: Effective thermal conductivity of lithium ceramic pebble beds for fusion blankets: a review. Fusion Sci. Technol. **47**(4), 1094–1100 (2005)

35. Springer, G.: Heat transfer in rarefied gases. Adv. Heat Transf. **7**, 163–218 (1971)

36. Vargas, W.L., McCarthy, J.: Conductivity of granular media with stagnant interstitial fluids via thermal particle dynamics simulation. Int. J. Heat Mass Transf. **45**(24), 4847–4856 (2002)

37. Dai, W., Pupeschi, S., Hanaor, D., Gan, Y.: Influence of gas pressure on the effective thermal conductivity of ceramic breeder pebble beds. Fusion Eng. Des. **118**, 45–51 (2017)

38. Gusarov, A., Kovalev, E.: Model of thermal conductivity in powder beds. Phys. Rev. B **80**(2), 024–202 (2009)

39. Slavin, A., Arcas, V., Greenhalgh, C., Irvine, E., Marshall, D.: Theoretical model for the thermal conductivity of a packed bed of solid spheroids in the presence of a static gas, with no adjustable parameters except at low pressure and temperature. Int. J. Heat Mass Transf. **45**(20), 4151–4161 (2002)

40. Hsu, C., Cheng, P., Wong, K.: Modified zehner-schlunder models for stagnant thermal conductivity of porous media. Int. J. Heat Mass Transf. **37**(17), 2751–2759 (1994)

41. Kanuparthi, S., Subbarayan, G., Siegmund, T., Sammakia, B.: An efficient network model for determining the effective thermal conductivity of particulate thermal interface materials. IEEE Trans. Compon. Packag. Technol. **31**(3), 611–621 (2008)

42. Kaganer, M.G.: Thermal Insulation in Cryogenic Engineering. Israel Program for Scientific Translations, Jerusalem (1969)

43. Adamson, A.: A Textbook of Physical Chemistry. Elsevier, Amsterdam (2012)

44. Negi, A., Anand, S.: A Textbook of Physical Chemistry. New Age International, Chennai (1985)

45. Wawryk, R., Rafalowicz, J.: The influence of residual gas pressure on the thermal conductivity of microsphere insulations. Int. J. Thermophys. **9**(4), 611–625 (1988)

46. Goodman, F.O.: Thermal accommodation coefficients. J. Phys. Chem. **84**(12), 1431–1445 (1980)

47. Wakao, N., Kato, K.: Effective thermal conductivity of packed beds. J. Chem. Eng. Jpn. **2**(1), 24–33 (1969)

48. Asakuma, Y., Kanazawa, Y., Yamamoto, T.: Thermal radiation analysis of packed bed by a homogenization method. Int. J. Heat Mass Transf. **73**, 97–102 (2014)

49. Cundall, P.A., Strack, O.D.: A discrete numerical model for granular assemblies. Geotechnique **29**(1), 47–65 (1979)

50. Johnson, K.: Contact Mechanics. Cambridge University Press, Cambridge (1985)

51. Jodrey, W., Tory, E.: Computer simulation of close random packing of equal spheres. Phys. Rev. A **32**(4), 2347 (1985)

52. Gan, Y., Kamlah, M.: Discrete element modelling of pebble beds: with application to uniaxial compression tests of ceramic breeder pebble beds. J. Mech. Phys. Solids **58**(2), 129–144 (2010)

53. Annabattula, R., Gan, Y., Kamlah, M.: Mechanics of binary and polydisperse spherical pebble assembly. Fusion Eng. Des. **87**(5), 853–858 (2012)

54. Scott, G., Kilgour, D.: The density of random close packing of spheres. J. Phys. D Appl. Phys. **2**(6), 863 (1969)

55. Aste, T.: Variations around disordered close packing. J. Phys. Condens. Matter **17**(24), S2361 (2005)

56. Löbbecke, B., Knitter, R., Rohde, M., Reimann, J.: Thermal conductivity of sintered lithium orthosilicate compacts. J. Nucl. Mater. **386**, 1068–1070 (2009)

57. Donne, M.D., Sordon, G.: Heat transfer in pebble beds for fusion blankets. Fusion Technol. **17**(4), 597–635 (1990)

58. Saito, S., Tsuchiya, K., Kawamura, H., Terai, T., Tanaka, S.: Density dependence on thermal properties of Li_2Tio_3 pellets. J. Nucl. Mater. **253**(1–3), 213–218 (1998)

59. Gierszewski, P.: Review of properties of lithium metatitanate. Fusion Eng. Des. **39**, 739–743 (1998)

60. Noda, K., Billone, M., Dienst, W., Flament, T., Lorenzetio, T., Roux, N.: Summary report for the ITER specialists meeting on blanket materials data base. ITER report (1990)

61. Liu, Y.Y., Tam, S.W.: Thermal conductivities for sintered and sphere-pac Li_2O and γ-$LiAlO_2$ solid breeders with and without irradiation effects. Fusion Sci. Technol. **7**(3), 399–410 (1985)

62. Petersen, H.: The Properties of Helium: Density, Specific Heats, Viscosity, and Thermal Conductivity at Pressures from 1 to 100 Bar and from Room Temperature to About 1800 K. Jul. Gjellerup, Copenhagen (1970)

63. Kadoya, K., Matsunaga, N., Nagashima, A.: Viscosity and thermal conductivity of dry air in the gaseous phase. J. Phys. Chem. Ref. Data **14**(4), 947–970 (1985)

64. Gierszewski, P.: Thermal conductivity of lithium metazirconate. Fusion Technol. **23**(3), 333–336 (1993)

65. Lide, D.R.: CRC Handbook of Chemistry and Physics. CRC Press, Boca Raton, 12J204 (2012)

Affiliations

Akhil Reddy Peeketi[1] · Marigrazia Moscardini[2] · Simone Pupeschi[2] · Yixiang Gan[3] · Marc Kamlah[2] · Ratna Kumar Annabattula[1]

✉ Ratna Kumar Annabattula
ratna@iitm.ac.in

1   Mechanics of Materials Laboratory, Department of Mechanical Engineering, Indian Institute of Technology Madras, Chennai 600036, India

2   Institute for Applied Materials (IAM), Karlsruhe Institute of Technology, 76344 Eggenstein-Leopoldshafen, Germany

3   School of Civil Engineering, The University of Sydney, Sydney, NSW 2006, Australia